Chem Soc Rev

Rechargeable redox flow batteries: Flow fields, stacks and design considerations

Journal:	*Chemical Society Reviews*
Manuscript ID	CS-SYN-01-2018-000072.R2
Article Type:	Review Article
Date Submitted by the Author:	19-Sep-2018
Complete List of Authors:	Ke, Xinyou; Case Western Reserve University Case School of Engineering, Mechanical and Aerospace Engineering Prahl, Joseph; Case Western Reserve University, Mechanical Engineering Alexander, Iwan; University of Alabama at Birmingham, School of Engineering Wainright, Jesse; Case Western Reserve University Case School of Engineering, Chemical and Biomolecular Engineering Zawodzinski, Thomas; University of Tennessee-Knoxville, Savinell, Robert; Case Western Reserve University, Department of Chemical Engineering

Rechargeable redox flow batteries: Flow fields, stacks and design considerations

Xinyou Ke[a,b*], Joseph M. Prahl[a], J. Iwan D. Alexander[c], Jesse S. Wainright[b,d], Thomas A. Zawodzinski[e,f*], and Robert F. Savinell[b,d*]

[a]Department of Mechanical and Aerospace Engineering, Case Western Reserve University, Cleveland, Ohio 44106, United States

[b]Electrochemical Engineering and Energy Laboratory, Case Western Reserve University, Cleveland, Ohio 44106, United States

[c]School of Engineering, University of Alabama at Birmingham, Birmingham, Alabama 35294, United States

[d]Department of Chemical and Biomolecular Engineering, Case Western Reserve University, Cleveland, Ohio 44106, United States

[e]Department of Chemical and Biomolecular Engineering, The University of Tennessee at Knoxville, Knoxville, Tennessee 37996, United States

[f]Oak Ridge National Laboratory, Oak Ridge, Tennessee 37830, United States

[*]Correspondence: xxk4@case.edu (Xinyou Ke), tzawodzi@utk.edu (Thomas A. Zawodzinski) and rfs2@case.edu (Robert F. Savinell)

Xinyou Ke's ORCID ID: https://orcid.org/0000-0003-1881-4873

J. Iwan D. Aelxander's ORCID ID: https://orcid.org/0000-0002-2384-7912

Jesse S. Wainright's ORCID ID: https://orcid.org/0000-0001-7902-7238

Thomas A. Zawodzinski's ORCID ID: https://orcid.org/0000-0002-2690-8784

Robert F. Savinell's ORCID ID: https://orcid.org/0000-0001-9662-2901

Abstract

Rechargeable redox flow batteries are being developed for medium and large-scale stationary energy storage applications. Flow batteries could play a significant role in maintaining the stability of the electrical grid in conjunction with intermittent renewable energy. However, they are significantly different from conventional batteries in operating principle. Recent contributions on flow batteries have addressed various aspects, including electrolyte, electrode, membrane, cell design, etc. In this review, we focus on the less-discussed practical aspects of devices, such as flow fields, stack and design considerations for developing high performance

large-scale flow batteries. Finally, we provide suggestions for further studies on developing advanced flow batteries and large-scale flow battery stacks.

Xinyou Ke is currently a Ph.D. candidate in the Department of Mechanical and Aerospace Engineering at Case Western Reserve University. He has worked with Professors Robert F. Savinell, Jesse S. Wainright and Joseph M. Prahl. Previously, he was trained at Massachusetts of Institute of Technology, Harvard University, Case Western Reserve University and South China University of Technology. His research focuses on exploring fundamentals on conduction mechanisms of slurry or semi-solid electrodes used for flow batteries, electrochemical flow capacitors and water treatments, and fundamental understanding of high performance flow batteries with flow field designs through both computational modeling and experimental approaches.

The late Joseph M. Prahl (recently passed away) was a full Professor in the Department of Mechanical and Aerospace Engineering (MAE) at Cases Western Reserve University (CWRU). Dr. Prahl received B.A. (1963), M.S. (1968) and Ph.D. (1968) in mechanical engineering all from Harvard University. During his Ph.D. studies, he worked with Professor Howard Wilson Emmons, who was called “the father of modern fire science”. Dr. Prahl was the department chair of MAE at CWRU for fifteen years and a backup Payload Specialist for the Space Shuttle Columbia mission STS-50 in 1992. His past research interests included fluid mechanics and thermodynamics.

J. Iwan D. Alexander has been Dean of the School of Engineering at the University of Alabama at Birmingham since August 2013. Dr. Alexander's research interests include the physics and mechanics of fluid interfaces, computational fluid mechanics, energy transport, crystal growth and solidification. He was a founding member of Case Western Reserve University's Great Lakes Energy Institute and became faculty director in 2007. He has worked with various NASA research programs since 1987 with NASA research programs and directed the USRA's National Center for Space Exploration Research from 2005-2010. Dr. Alexander was awarded NASA's Exceptional Service Medal in August 2008.

Jesse S. Wainright is a Research Professor in the Department of Chemical and Biomolecular Engineering at Case Western Reserve University (CWRU) in Cleveland, United States. Prior to joining CWRU, Dr. Wainright spent seven years on the research staff at the Standard Oil Company. While a research faculty member at CWRU for the past twenty-four years and has published over sixty journal articles, primarily devoted to polymer electrolyte membranes, fuel cells and aqueous batteries. He is currently co-P.I. with Prof. Robert F. Savinell for CWRU's efforts in flow battery research, with funding from NSF, DOE and ARPA-E.

Thomas A. Zawodzinski is the Governor's Chair Professor with a joint appointment at The University of Tennessee at Knoxville and Oak Ridge National Laboratory. Dr. Zawodzinski was the F. Alex Nason Professor of Engineering at Case Western Reserve University (CWRU), Director of the CWRU Advanced Power Institute and the Ohio Eminent Scholar in fuel cells. Dr. Zawodzinski was the former team leader for fuel cells at Los Alamos National Laboratory for thirteen years. His research focuses on fundamental science and application of electrolytes, electrodes and membranes for fuel cells, flow batteries, batteries, electrochemical reactors and other energy storage systems.

Robert F. Savinell is Distinguished University Professor and the George S. Dively Professor of Engineering at Case Western Reserve University (CWRU). Dr. Savinell was the director of the Ernest B. Yeager Center for Electrochemical Sciences at CWRU for ten years and served as Dean of Engineering at CWRU for seven years. Dr. Savinell has been engaged in electrochemical engineering research and development for over forty years. His research is directed at fundamental science and mechanistic issues of electrochemical processes, electrochemical system design and development, modeling and optimization.

1. Introduction

Redox flow batteries (RFBs) are being developed for medium and large-scale stationary energy storage applications [1-6]. Along with storage of electricity generated from intermittent renewable energy resources, such as solar, wind and tide energy, RFBs provide a potential ability to enhance the stability of the grid [7-9]. RFBs can shift electric energy from off-peak demand periods (i.e. nighttime) to peak demand periods (daytime) [10]. This function of peak-shaving is critical to maintain stable electric balance for urban's utilization.

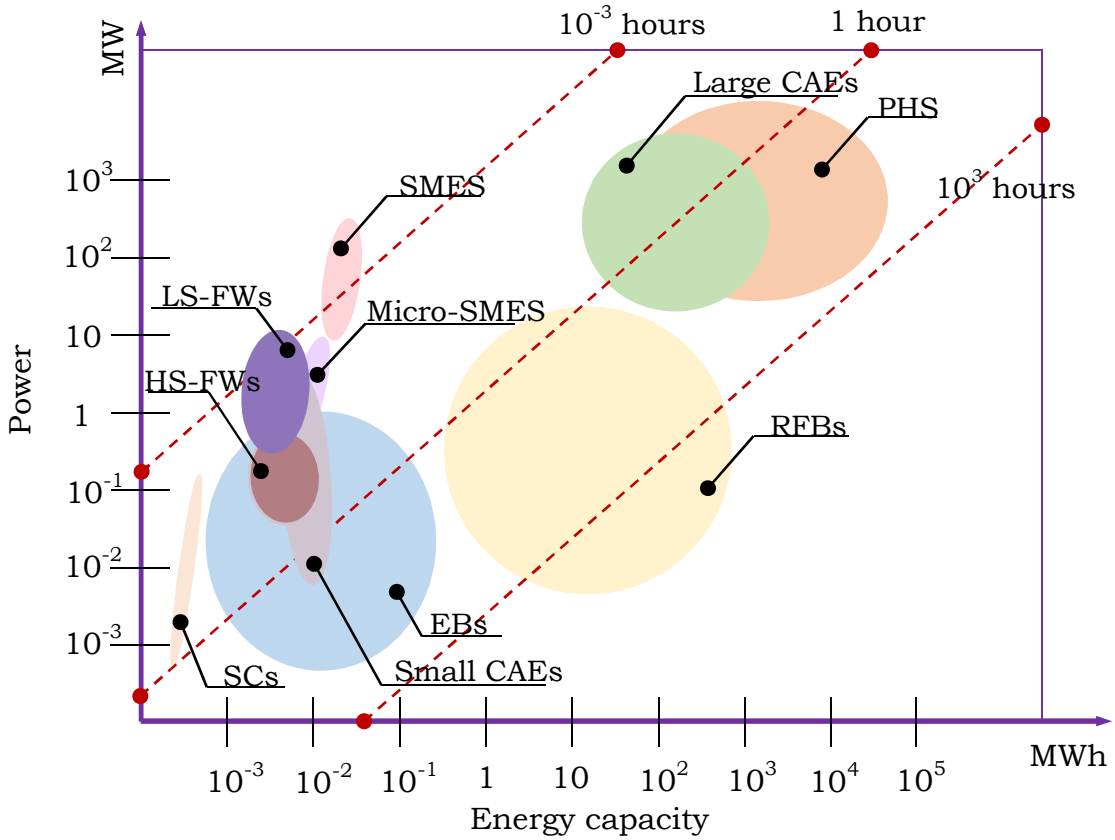

PHS: Pump hydro storage; CAEs: Compressed air energy storage; RFBs: Redox flow batteries; SCs: Supercapacitors; LS-FWs: Low speed flywheels; HS-FWs: High speed flywheels; SMEs: Superconducting magnetic energy storage; EBs: Electrochemical batteries

Figure 1 Comparisons of power output and energy stored among various electrochemical systems. Redrawn from ref. 10.

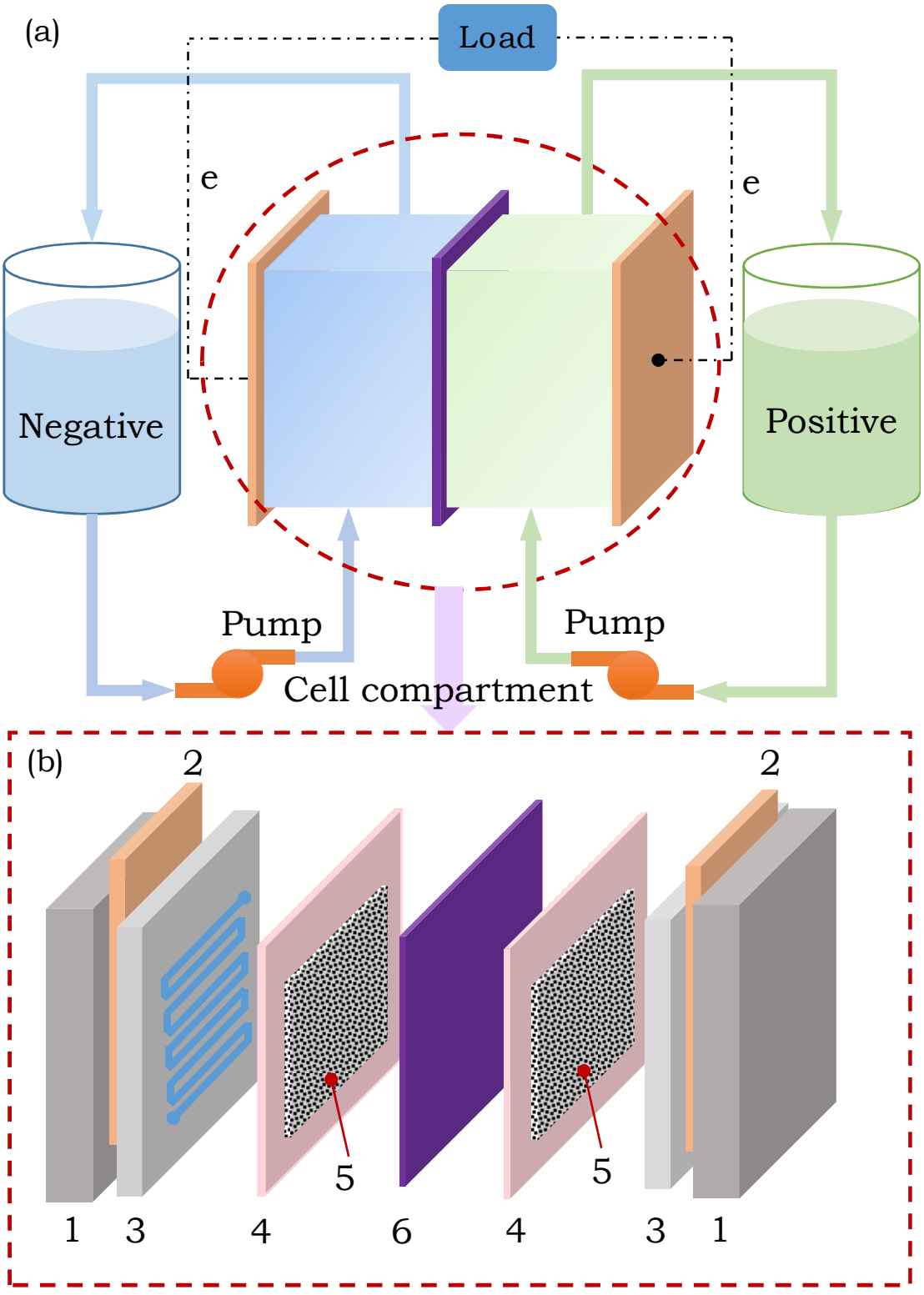
(a)
Load
e
e
Negative
Positive
Pump
Pump
Cell compartment
(b)
2
2
5
5
1
3
4
6
4
3
1

Figure 2 (a) Schematic of a typical flow battery and (b) A detailed-diagram of cell compartment in flow batteries with a flow field design, main components include: 1-endplates, 2-current collectors, 3-graphite plates engraved with a serpentine flow field, 4-gaskets, 5-porous electrodes, and 6-ion exchange membrane. Redrawn from ref. 100.

Compared with supercapacitors and solid-state batteries, flow batteries store more energy and deliver more power as shown in Fig. 1. Although compressed air and pumped hydro energy storage have larger energy capacities in comparison to RFBs, environmental impact and geography are limiting issues for these technologies. Fig. 2 (a) introduces the working principle of flow batteries: dissolved electro-active materials are stored in the external electrolyte reservoirs and circulated into the cell compartment by the pumps. During charge and discharge, the flowing electrolyte delivers electroactive reagents into the cell compartment to generate/consume electrons at the electrode surfaces. The electrons are eventually transferred from the current collectors to and from the external load. In this way chemical and electrical energy are directly interconverted.

To date, various types of RFBs have been developed typically sorted by their different chemistries. Common varieties include all-vanadium [11-16], zinc-bromine [17-21], hydrogen-bromine [22,23], all-iron [24-29], all-iron slurry [30-32], semi-solid lithium [33-41], all-copper [42-46], zinc-polyiodide [47,48], lithium-iodine [49,50], organic [51-59], polymer [60-62], alkaline [63-65], biomimetic [59], zinc-cerium [67,68], combined flow battery with solar energy [69-72] and other non-aqueous systems [73-76]. Features such as low capital cost, environmentally benign chemistry, long-term stability and high electrochemical performance are critical considerations for developing next-generation flow batteries. Some of the aforementioned chemistries fall short on one or more of those considerations.

Recently, more effort has been paid to improving cell performance for a spectrum of chemistries by improving various aspects of the cell design and components, including electrode structure [77-83], electrolyte [47-59, 73-76], membrane [84-89] and cell architecture design [90-134]. Flow field designs used in flow batteries have interested many researchers and engineers since 2012. Zawodzinski's group [90] first reported a vanadium flow battery (VRB) with a "zero-gap" serpentine flow field design, which is similar to those used in proton exchange membrane (PEM) fuel cells. Improved limiting current density and peak power density (multiple times higher) were demonstrated as compared with the earlier flow battery designs without flow fields where electrolyte enters a long channel packed with a porous electrode. Other experimental results also showed that RFBs with flow field designs exhibit better electrochemical performance compared with those without flow field designs. For example, it was found that VRB with a serpentine flow field had a higher round trip efficiency compared with the one without flow field structure [92]. An interdigitated flow field over multiple layers of carbon paper electrode resulted in a lower ohmic loss compared with earlier flow battery designs without flow fields [95]. One explanation of the improved cell performance is that thinner carbon paper electrodes (e.g. hundred microns) instead of carbon felt or graphite felt electrodes (e.g. several millimeters) are enabled by the flow field designs and this consequently leads to smaller ohmic loss. This 'ohmic loss' is the combination of the losses associated with electronic resistance through the porous electrode and the ionic resistance through the electrolyte within the porous electrode. These resistances are in parallel and by having a thin electrode, the ohmic loss can be reduced. In addition, carbon paper electrodes also have a large surface area to volume ratio, which also reduces kinetic and mass transport losses. The total combined 'ohmic loss', kinetic and mass transport losses, and the membrane resistance loss results in an apparent direct

current (DC) area specific resistance (ASR) measured in a cell. Typically, the porous electrode thickness is ~ 200 μm for a single layer of Tory paper electrode [91], ~ 400 μm for a single layer of SGL paper electrode [90,94] and ~ 3 mm for carbon felt electrode or graphite felt electrode [99]. The thickness of the porous electrode is smaller after compression in an assembled cell, and the compression ratio is typically ~ 25 %. A schematic of a typical flow battery with a serpentine flow field design over the porous electrode is shown in Fig. 2 (b). The serpentine flow field design originally evolved from the proton exchange membrane fuel cell (PEMFC) design [135-139] which in turn borrowed the design from phosphoric acid fuel cell designs. For the serpentine flow channel over the porous electrode layered system, the electrolyte is forced to flow through the flow channel and over the porous electrode, and a portion of electrolyte penetrates into the porous electrode driven by pressure gradients. It was proposed that the cell performance with a serpentine flow field may be associated to the stoichiometric availability of electrolyte reactant penetration into the porous electrode [99-103]. Other flow fields, e.g. interdigitated [93,95,105,106], parallel [92,131], were also reported in flow batteries. However, a thorough understanding of cell performance measured by globalized results, i.e. polarizations, efficiencies, discharged capacities, as they are related to localized phenomena, i.e. flow distributions, potential and current distributions, is still under development for RFBs single cells and stacks.

The motivation for this review is to provide background and a basis for researchers and engineers to further study the influence on RFB cell performance associated with flow field designs, including their implementation in stacks. Various aspects will be surveyed, such as types of flow field architectures, flow distribution, cell performance, large-scale stack designs and commercial systems, stack performance, optimization of non-uniform flow distributions,

shunt currents, localized current distributions, and limiting and maximum current densities. Several review papers [1-4, 6-7, 140-150] on flow batteries have been published, but this work is distinguished by its primary focus on flow fields, stacks and design considerations of RFBs.

2. Redox flow batteries with flow field architectures

2.1 Classic flow field structures

Typical flow field designs used in RFBs are the serpentine flow field (SFF) and interdigitated flow field (IFF). The structures of SFF and IFF over the porous electrode are shown in Fig. 3. It can be seen that the electrolyte flow can be forced through the porous electrode and adjacent flow channels for both SFF and IFF. The difference between them is that only a small fraction of the electrolyte reactants actually penetrates into the porous electrode for an ideally behaved SFF while all of the electrolyte reactants are forced through the porous electrode for the IFF. From the aspect of stoichiometric availability of reactant with the porous electrode, the IFF should be better than the SFF. However, non-uniform flow distributions and larger pressure drops/pump losses are more serious issues for IFF if not designed properly. There is no general agreement on which design is better, i.e. SFF vs. IFF. According to the reference [105], the SFF is better than IFF for a certain range of entrance volumetric flow rates. It is likely, however, that the optimum flow field depends on other aspects of the system. For example, it may involve trade-offs with the properties of the electrode material chosen. Other flow fields, i.e. parallel flow field (PFF) [131] and spiral flow field (sFF) [104] or tubular flow field (TFF) [123] or circular flow field (CFF) [128] also have been mentioned as possible for applications in flow batteries. Examples of in-house flow field designs used in laboratory-prototype flow batteries of Case Western Reserve University (CWRU) are shown in Fig. 4 (a)-(d), which represent SFF design for 5 cm^2 cell, IFF design for 9 cm^2 cell, SFF design for 50 cm^2 cell and IFF design for 50 cm^2, respectively.

Typically, the ratio of channel width over landing width is 1−2. But, dimensions and layouts of flow fields can be re-designed, and this should be based on the manufacturing convenience, size of flow cell and desired or optimized cell performance, etc.

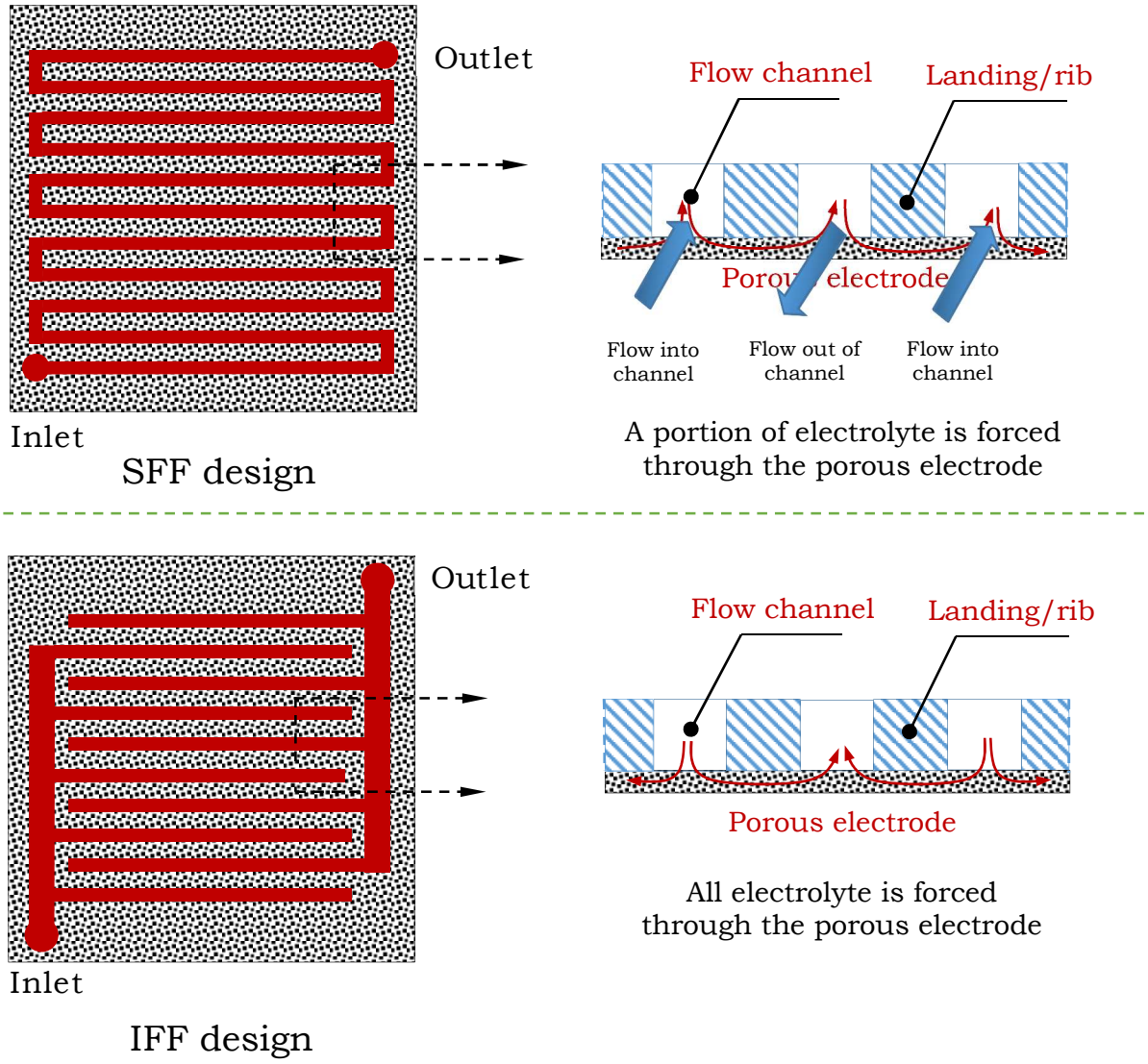

Figure 3 Two typical flow fields used in flow batteries: serpentine flow field (SFF) and interdigitated flow field (IFF).

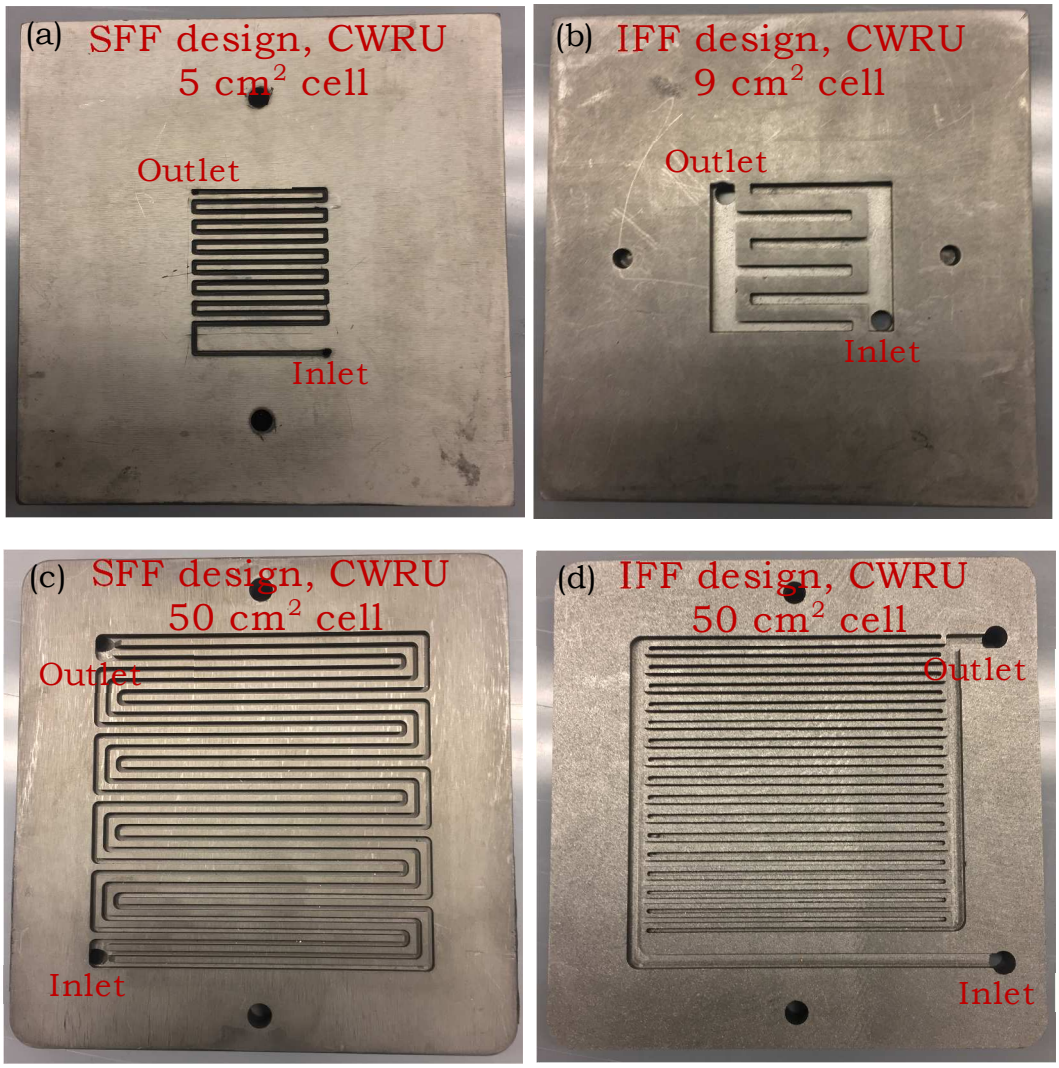

Figure 4: Several types of flow field designs used in the flow batteries in the Electrochemical Engineering Energy Laboratory of Case Western Reserve University: (a) SFF design for 5 cm^2 cell (channel width: 1 mm, landing width: 0.5 mm and channel depth: 1 mm), (b) IFF design for 9 cm^2 (channel width: 2.5 mm, landing width: 2 mm and channel depth: 3 mm), (c) SFF design for 50 cm^2 cell (channel width: 1 mm, landing width: 1 mm and channel depth: 1 mm) and (d) IFF design for 50 cm^2 cell (channel width: 1 mm, landing width: 1 mm and channel depth: 1 mm). (Photo courtesy of Professors Robert F. Savinell, Jesse S. Wainright and Nicholas Sinclair from Case Western Reserve University (CWRU)).

2.2 Comparisons: "Flow-through" & "flow-by" electrode configurations

Fig. 5 (a) depicts the classic two-dimensional "flow-through" electrode configuration used in RFBs. This type of electrode design has been widely studied [151-168]. A two-dimensional "flow-by" electrode configuration as shown in Fig. 5 (b) used in flow batteries with flow field designs, i.e. SFF, evolved from proton exchange membrane (PEM) fuel cell design. For both RFBs with "flow-through" and "flow-by" electrode designs, the main electrolyte flow is perpendicular to the current flow. However, it should be noted that earlier literature on the distinction between "flow-through" and "flow-by" electrode structures was related to the directions of electrolyte flow and current flow [166,167]: "flow-through" meant fluid flow was parallel to the current flow and "flow-by" meant fluid flow was perpendicular to the current flow. These definitions are not used in our discussions. In cases discussed here, fluid flow is perpendicular to the current flow in both types of "flow-through" and "flow-by" electrode configurations here. As shown in Fig. 5, the porous electrode, i.e. carbon felts, used in the "flow-through" design is always thicker than the porous electrode, i.e. carbon paper, used in the "flow-by" design. Improved cell performance associated with the smaller ohmic loss has been demonstrated in RFBs with "flow-by" electrodes. In reality, we are referring only to the nominal direction of flow. As fluid penetrates the porous electrode, the internal structure of the electrode leads to components of transport in all directions.

2.3 Other new flow field designs

More recently, several new types of field designs have been reported for flow batteries. Houser et al. [106] developed equal path length (EPL) and aspect ratio (AR) flow fields, which are evolutions of designs of the interdigitated flow fields (IFF). As noted, for IFF all electrolyte flow is forced through the porous electrode. Higher cell performance in both EPL and AR was

achieved as compared with SFF and IFF based on the observed polarization curves. A corrugated flow field (CFF) [108] was designed for enhancing the localized mass transfer in the porous electrode and this design leads to higher limiting current density and peak power density. A tapered, micro-scale-interdigitated flow field (T-IFF, see Fig. 6 (a) and (b)) [109] was fabricated by 3D printing. In this innovative approach, the flow battery supplies power but its fluid also carries waste heat from the electronic devices, i.e. microprocessors. For such a flow battery with micro-fabricated flow structure can output a peak power density of 0.99 W cm^{-2}.

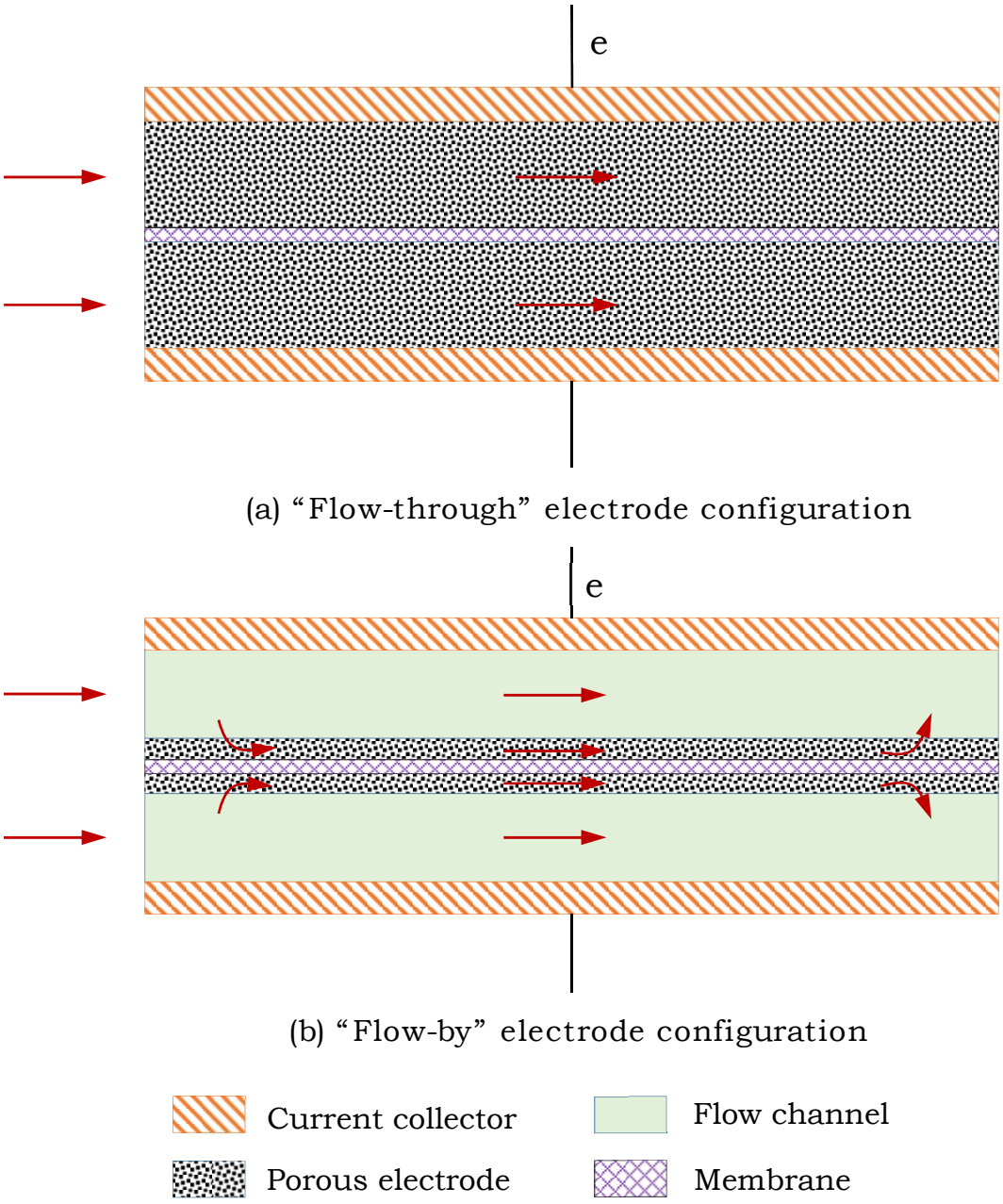

Figure 5 Configurations of two-dimensional configurations of porous electrodes used in RFBs: (a) “flow-through” design and (b) “flow-by” design. Redrawn from ref. 102.

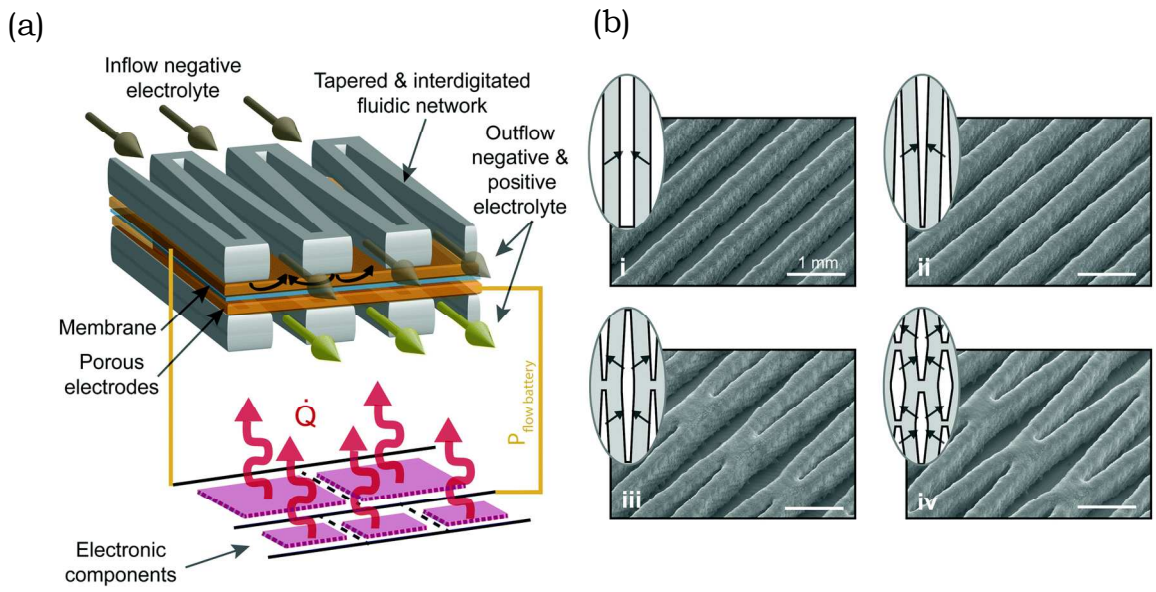

Figure 6 (a) Tapered-interdigitated flow field (T-IFF) design in a miniaturized redox flow cell (RFC). (b) Scanning electron micrographs (SEMs) of the 3D-printed T-IFF configurations (scale bar: 1mm), four different designs were reported: (i) straight flow channels with a single-pass, (ii) tapered flow channels with a single-pass, (iii) tapered flow channels with a dual-pass and (iv) tapered flow channels with a quadruple-pass. Reprinted with permission from ref. 109, Copyright 2017, The Royal Society of Chemistry.

2.4 Summary: Improved performance with flow field designs

Various studies on high performance achieved in RFBs using flow field designs have been reported. A summary of types of flow field design, limiting current density, peak power density, types of RFBs and main experimental conditions is summarized in Table 1. The reported normalized limiting current density achieved in flow batteries with flow field designs can be larger than 17,500 mA cm^{-2} mol^{-1} and peak power density can reach to around 2,600 mW cm^{-2}, both densities are based on the membrane area.

Table 1 Summary for the limiting current density and peak power density achieved in RFBs with various flow field designs

Flow field structures	Normalized limiting current density ($mA\ cm^{-2}\ mol^{-1}$)	Peak power density ($mW\ cm^{-2}$)	Types of RFBs	Main experimental conditions	References
SFF	750	557	Vanadium flow battery	5 cm^2 cell design; 1 M Vanadium, 4 M H_2SO_4; three layers of SGL 10 AA carbon paper electrode; Nafion 117 membrane; entrance volumetric flow rate of 20 $cm^3\ min^{-1}$; SOC= 60 %	[90] 2012
SFF	955	767	Vanadium flow battery	5 cm^2 cell design; 1 M Vanadium, 5 M H_2SO_4; three layers of SGL 10 AA carbon paper electrode; Nafion 212 membrane; entrance volumetric flow rate of 90 $cm^3\ min^{-1}$; SOC= 54 %	[91] 2012
SFF	> 2,500	1,400	Hydrogen-Bromine flow battery	10 cm^2 cell design; 0.9 M Br_2, 1 M HBr; three layers of SGL 10 AA carbon paper electrode; Nafion 212 membrane; entrance volumetric flow rate of 300 $cm^3\ min^{-1}$	[110] 2012
SFF	763-924	424-557	Vanadium flow battery	5 cm^2 cell design; 1 M Vanadium, 4 M H_2SO_4; three layers of SGL 10 AA carbon paper electrode after laser-perforated treatment; Nafion 117 membrane; entrance volumetric flow rate of 20 $cm^3\ min^{-1}$ to 120 $cm^3\ min^{-1}$	[94] 2013
IFF	> 1,800	1,300	Vanadium flow battery	NA	[93] 2013
IFF	> 1,200	600	Quinone-Bromine flow battery	2 cm^2 cell design; 1 M AQDS, 1 M H_2SO_4 (negative), 3 M HBr, 0.5 M Br_2 (positive); six layers of Toray carbon paper electrode; Nafion 212; entrance volumetric flow rate of 200 $cm^3\ min^{-1}$; SOC= 90 %	[45] 2014
SFF	> 1,200	700	Alkaline-Quinone flow battery	5 cm^2 cell design; 1 M 2,6-DHAQ, 3 M potassium electrolyte (negative), 0.8 M ferrocyanide, 4.2 M potassium electrolyte (positive); three layers of SGL 10 AA carbon paper electrode; Nafion 212; entrance volumetric flow rate of 60 $cm^3\ min^{-1}$; SOC= 100 %	[57] 2015
SFF	> 1,200	350	Alloxazine-based organic flow battery	5 cm^2 cell design; 0.5 M alloxazine 7/8-carbonxylic acid (ACA) (negative), 0.4 M ferrocyanide, 40 mM ferricyanide (positive); two or three layers of SGL 10 AA carbon paper electrode; Nafion 212; entrance volumetric flow rate of 60 $cm^3\ min^{-1}$; SOC= 100 %	[48] 2016
SFF	> 190	60	Neutral pH Organic-Organometallic flow battery	5 cm^2 cell design; 1.3 M BTMAP-Vi (negative), 1.3 M BTMAP-Fc (positive); four layers of SGL 39A carbon paper electrode; Selemion DSV membrane; entrance volumetric flow rate of 60 $cm^3\ min^{-1}$; SOC= 100%	[49] 2017
EPL	> 645	1,200-1,400	Vanadium flow battery	9 cm^2 cell design; 1.7 M vanadyl sulfate, 3.3 M sulfuric acid; 10 AA carbon paper electrode (nominal thickness: 410 μm); Nafion 117; entrance volumetric flow rate of 50 $cm^3\ min^{-1}$; SOC=50 %	[106] 2017
AR	> 585	1,000-1,200			
cFF	> 15,000	1,200	Alkaline-based flow battery	1 cm^2 cell design; 0.2 M 2,6-DHAQ, 2 M KOH (negative), 0.4 M $K_4Fe(CN)_6$, 1 M KOH (positive); Spectracarb 2050A-1050 porous electrode; Nafion 115; entrance volumetric flow rate of 300 $cm^3\ min^{-1}$	[108] 2017

T-IFF	> 17,500	1,400	Alkaline-based flow battery	0.2 M 2,6-DHAQ, 2 M KOH (negative), 0.4 M $K_4Fe(CN)_6$, 1 M KOH (positive); Spectracarb 2050A-1050 porous electrode; Nafion 211; entrance volumetric flow rate of 300-400 cm^3 min^{-1}	[109] 2017
SFF	2,961	2,588	Vanadium flow battery	5 cm^2 cell design; 1.7 M Vanadium, 5 M H_2SO_4; one layer of SGL 10 AA carbon paper electrode; SDAPP 2.3 membrane; entrance volumetric flow rate of 90 cm^3 min^{-1}; SOC= 100 %	[169] 2018

Note: SFF: serpentine flow field, IFF: interdigitated flow field, EPL: equal path length, AR: aspect ratio, cFF: corrugated flow field and T-IFF: tapered-interdigitated flow field

The literature summarized in Table 1 indicates that several main advantages of RFBs with flow field designs have been demonstrated. These include: (1) lower ohmic loss, because of thinner carbon paper electrode used instead of thicker carbon felt electrode or graphite felt electrode; (2) enhanced localized mass transfer in the porous electrode, because the electrolyte flow is driven through the porous electrode by the forced convection associated with pressure drop along the flow fields, and (3) consequent improved cell performance, higher limiting current density and peak power density are achieved due to lower ohmic loss and enhanced localized mass transfer. However, some critical issues related to transport phenomena arise. These include additional pressure drops/pump losses and the lack of uniformity of electrolyte flow distributions, often contributing to localized non-uniform potential and current distributions. The flow distributions affect the reactant utilization through the porous electrode. Non-uniform flow distributions lead to incomplete utilization of the internal surface of the electrode, causing a decrease in cell performance and sometimes adversely affecting durability of the electrode. Localized current distributions within the porous electrode are reflections of the utilization of the electrode. Uniform localized current distributions within the porous electrode are desired to reduce ohmic and kinetic losses. Limiting current density is one important criteria to evaluate the cell performance of flow batteries but, as implied by the discussion above, these non-uniformities will also be reflected in pseudo-ohmic losses at intermediate current density as well. Increasing operating and limiting current densities are always desired for developing high performance flow batteries for high performance.

3. Understanding transport phenomena in flow batteries with flow fields

Examining transport phenomena in RFBs with flow field designs can contribute to a better understanding of improved cell performance, such as current density and power density, and

possible approaches for further optimizations of RFBs. As noted above, the coupling between electrode and electrolyte flow is an important element to understand. As the electrolyte flows through the flow fields and over the porous electrode, forced convection (due to pressure gradient), diffusion (due to concentration gradient) and migration (due to potential gradient) terms are in effect. From the aspect of fluid dynamic modeling, the Navier-Stokes equation [170] is applicable to study the flow patterns and distributions for Newtonian electrolytes through the flow fields under forced convection. The Brinkman-Darcy equation [171] can be used to describe the flow physics for the electrolyte flow through the porous electrode for Newtonian electrolytes. From the aspect of electrochemical modeling, the Nernst-Planck equation [172] correlates the reactant flux with the convection, diffusion and migration terms for the diluted solutions. Newman et al. [172] also pointed out that a modified Nernst-Planck equation may be applicable for the concentrated solutions. Other useful equations [155,157] also need to be considered for a full model include Ohm's law, material balance equation, conservation of charge, the Nernst equilibrium equation, and the Bulter-Volmer (or alternative) kinetic equation embedded with chemical kinetic mechanistic terms. A common oversimplification in electrochemical models is the blind application of the Butler-Volmer expression with the net number of electrons from the reaction rather than the proper kinetic expression. Both fluid dynamic and electrochemistry modeling are desired to fully understand the transport phenomena in RFBs with flow field designs.

3.1 Porous electrode: Porosity, permeability and specific surface area

Knowledge about the physical properties of a porous electrode, such as porosity, permeability and specific surface area, is essential to the modeling of the porous electrode used in RFBs. Various types of porous electrode have been used in RFBs with flow field designs, such as i.e.

SGL 10AA and other related carbon papers, Toray carbon paper and innumerable carbon felts. Literature on experimental value of porosity, permeability and specific surface area on those porous electrodes used in RFBs is quite limited. However, several models have been developed to correlate the permeability with porosity of porous electrode as shown in Fig. 7 (a) and the details on those models are summarized in Table 2.

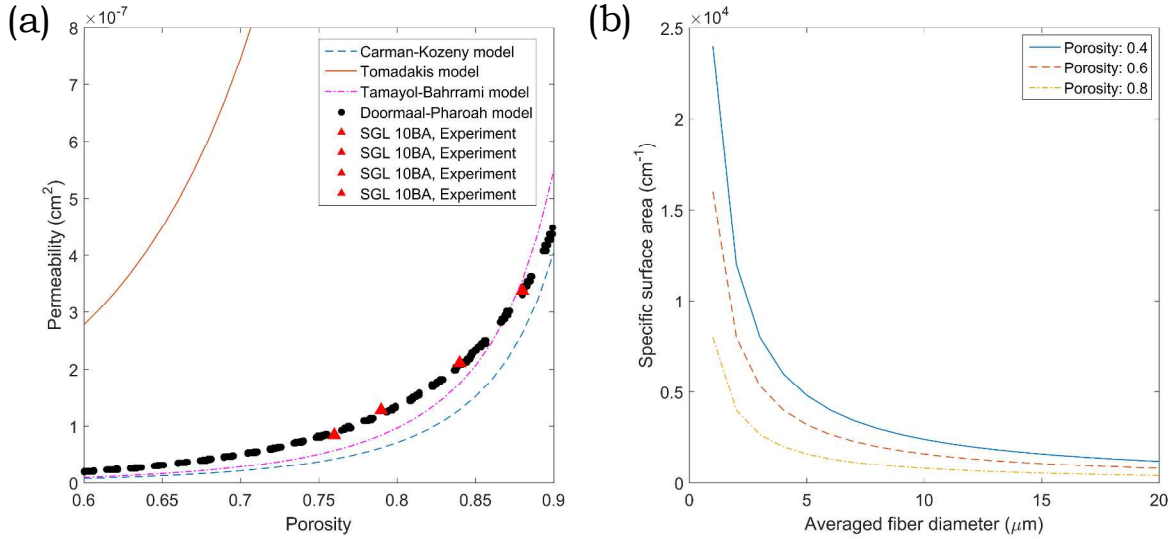

Figure 7 (a) Comparisons between predictions of permeability vs. porosity from several models: Carman-Kozeny [177,178], Tomadakis [179], Tamayol-Bahrami [173] and Doormaal-Pharoah [174] and experimental data [175,176] for SGL 10BA carbon paper electrode. Redrawn from ref. 103. (b) Estimated specific surface area vs. fiber diameter with various porosities from Carta et al.'s model [180].

It was found that predictions of flow permeability from the models developed by Tamayol and Bahrami [173] and Doormaal and Pharoah [174] match better with the experimental data [175,176] as compared to the Carman-Kozeny model [177,178] and a model developed by Tomadakis [179]. One possible explanation for the prediction by the Tomadakis model being significantly different to other three models is that the derivation of this model was based on

Archie' s law [179] instead of classic Darcy' s law. Also, a possible explanation for a larger discrepancy between the predictions by Carman-Kozeny model and experimental data compared with the predictions by Tamayol-Bahrami model and Doormaal-Pharoah model is that Carman-Kozeny model mainly assume spherical particles and do not consider the particle-particle contact area. While, the Tamayol-Bahrami and Doormaal-Pharoah models do consider the area of contacts of overlapping fibers. All the models mentioned above only consider ideal particles or aligned porous fibers, and other irregular porous fiber shapes are not taken into account. Therefore, advanced models for predicting the permeability of porous materials with various shapes are still desired.

Table 2 Details on models for correlating the permeability and porosity of porous electrode.

Permeability	Expressions	Descriptions	Sources
$k=$	$\frac{{d_f}^2\boldsymbol{\varepsilon}^3}{C_{ck}(1-\boldsymbol{\varepsilon})^2}$	Carman-Kozeny model C_{ck}=180 *Mainly assume uniform distributed spherical particles without contact*	[177,178]
	$\frac{{d_f}^2\boldsymbol{\varepsilon}(\boldsymbol{\varepsilon}-\alpha_1)^{(\alpha_2+2)}}{2(ln\boldsymbol{\varepsilon})^2(1-\alpha_1)^{\alpha_2}(\alpha_2\boldsymbol{\varepsilon}+\boldsymbol{\varepsilon}-\alpha_1)^2}$	Tomadakis model α_1=0.037, α_2=0.661 *Assume random aligned fibers with contact*	[179]
	$0.012{d_f}^2\boldsymbol{\varepsilon}\left(\frac{\pi^2}{16(1-\boldsymbol{\varepsilon})}-\frac{\pi}{2(1-\boldsymbol{\varepsilon})}+1\right)\left(1+0.72\frac{1-\boldsymbol{\varepsilon}}{(\boldsymbol{\varepsilon}-0.11)^{0.54}}\right)$	Tamayol-Bahrami (T-B) model *Assume random aligned fibers with contact*	[173]
	No explicit form Computed by Lattice Boltzmann method	Doormaal-Pharoah (D-P) model *Assume random aligned fibers with contact*	[174]

It was also pointed out [103] that the porosity and permeability of porous electrode were also affected by the degree of compression during the assembly of the flow cell. A larger level of compression leads to lower porosity and reduced permeability. For predicting the specific surface area of porous electrode, a simplified filament analogue model was developed by Carta et al. [180]. This model correlates the specific surface area with porosity and averaged diameter of ideal cylinder porous fibers. Fig. 7 (b) shows the relationships between the specific surface area and averaged fiber diameter with different porosity estimated by Carta et al.'s model. From this correlation, it can be seen that a lower porosity and a smaller averaged fiber diameter will lead to a larger specific surface area. Weber et al. [2] pointed out that the actual surface area may be less than that predicted by Carta et al.'s model, because the porous fibers contact and overlap each other in an actual porous electrode. Also, the estimations by Carta et al.'s model may result in large errors if the shape of porous fibers is significantly different from the ideal cylinder. The Brunauer-Emmett-Teller (BET) experimental method [181,182] determines the specific surface area of porous materials by using the adsorption and de-sorption of gas molecules, e.g. nitrogen, on the surfaces of porous materials. The pore size distributions of porous materials also can be measured by multi-point BET. However, it is the electrochemically active or accessible surface area rather than the specific surface area of porous electrode that is closely related to the performance of a working flow battery. The active surface area reflects both the access of electrolyte reactants to internal surfaces of a porous electrode as well as specific surface area as a physical property of a porous electrode. It should be noted that the active surface area is always smaller than the specific surface area. The accessible surface is a complex function of internal pore geometry and size as well as the surface energy of the electrode material. Each of those factors influence the wettability of the surface. Even if all of the above are taken into account,

under operating conditions the electrode volume may not be fully accessed. Non-uniformity of electrolyte flow distributions is a significant factor that affects the materials' utilizations. For some extreme cases, "dead zones" (lack of electrolyte) within the porous electrode strongly reduce the unitization of porous electrode, resulting in reduced performance of RFBs. In a later section, flow distributions and optimizations designed to enhance uniformity will be discussed.

3.2 Flow dynamic modeling

Modeling of flow distributions in RFBs helps to understand the utilizations of electrolyte reactants through the porous electrode. However, flow distributions in RFBs are almost impossible to be measured directly through the experimental methods. It has been demonstrated that computational fluid dynamics (CFD) is an effective approach to simulate the electrolyte flow transport through the flow field and porous electrode in RFBs [99]. Though CFD is useful, when considering such modeling results, it is wise to seek or keep in mind experimental results and the degree to which a given CFD model is validated. For most aqueous electrolytes used in RFBs, the electrolyte flow is considered as incompressible and Newtonian fluid. For some "very viscous" electrolytes used in non-aqueous flow batteries [26,27,73-76,128], the electrolyte flow should be considered as non-Newtonian fluid. Early work on two-dimensional (2D) flow dynamics in RFBs with a single flow channel over the porous electrode was reported by Ke and Savinell et al. [100-102]. The single flow channel-porous electrode layered system is sandwiched among the current collector, graphite plate and membrane as shown in Fig. 8 (a). The electrolyte flow develops from an entrance flow profile to developing and fully developed flow profiles as shown in Fig. 8 (b). It was demonstrated that, due to low permeability of porous electrode, flow velocity in the porous electrode is much smaller than fluid flow in the flow channel (see Fig. 8

(b)). The volumetric flow penetration through the porous electrode reflects the availability of electrolyte reactants within the porous electrode and consequently affects the cell performance.

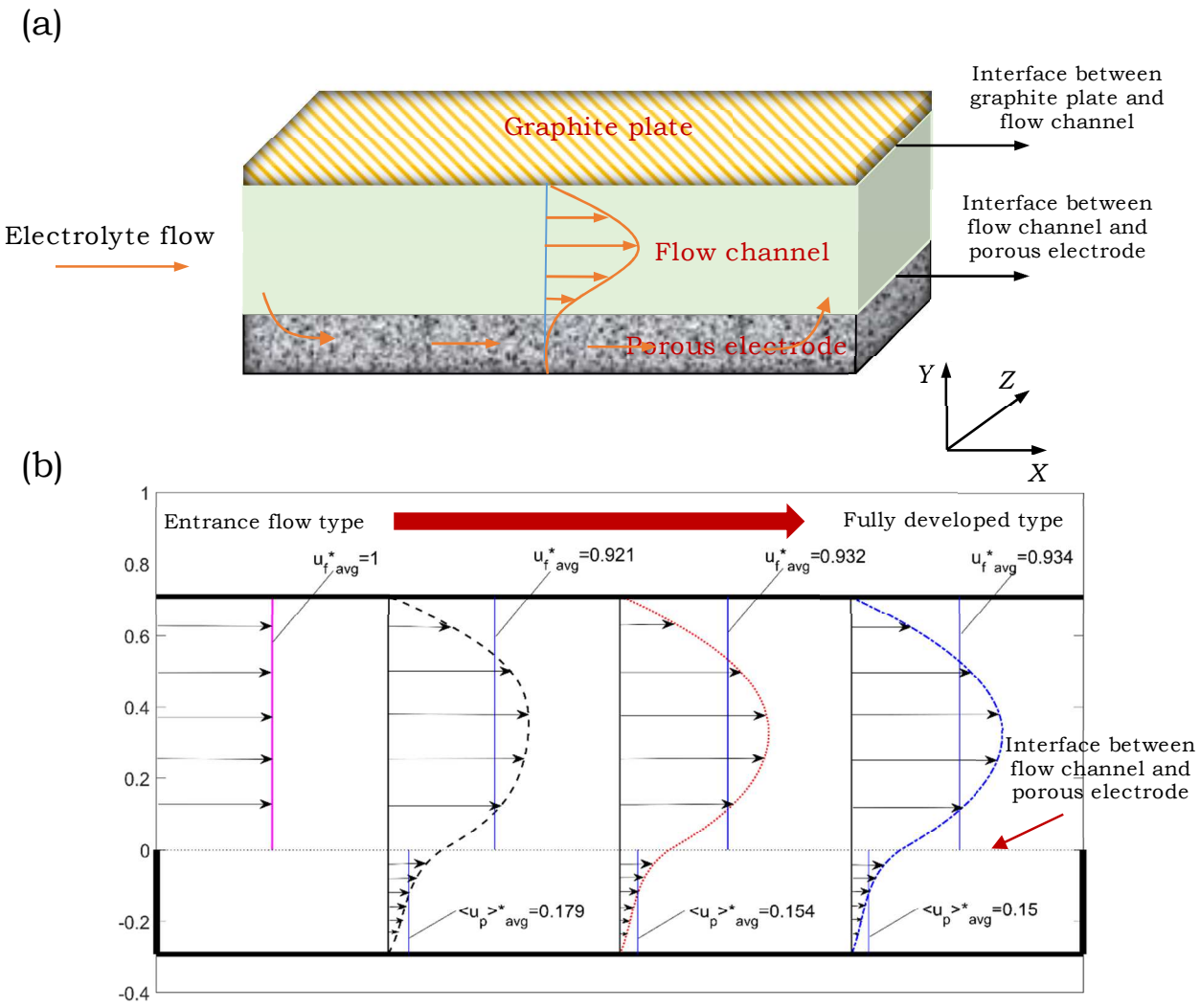

Figure 8 (a) Diagram of electrolyte flow through a single flow channel and over the porous electrode in RFBs and a portion of electrolyte flow is penetrated into the porous electrode at the interface between the single flow channel and porous electrode. Redrawn from ref. 99. (b) Two-dimensional flow distributions in the flow channel-porous electrode layered system (permeability: 9.7×10^{-9} m^2, porosity: 0.78 and Reynold number: 91.5) as electrolyte flow

develops from the ideal plug flow entrance type to the fully developed regime in the flow channel and porous electrode. Reprinted with permission from ref. 100, Copyright 2014, Elsevier.

Compared with the 2D flow dynamics, simulations of three-dimensional (3D) flow dynamics in a SFF gives a better understanding of cell performance. For example, the significant effect of landings/ribs in RFBs with serpentine flow fields on flow penetration through the porous electrode is not able to be captured by the 2D flow dynamic simulations by only considering a single flow channel over the porous electrode [102]. The flow penetration occurs at the interface between the flow field and porous electrode, and an example is given by Fig. 9, which describes the localized flow penetration at the interface between a serpentine flow field and a porous carbon electrode. The red color represents the flow penetration out of the interface, and the blue color represents the flow penetration into the interface. It is clear that the localized flow penetration is not uniform, and more flow penetration occurs in the region near to the entrance and much less flow penetration occurs in the region near to the outlet. The non-uniform flow distributions can result in non-uniform reactions and localized current distributions. Optimization of flow distributions within the porous electrode is significant to achieve uniformly localized current distributions and consequently improved cell performance. CFD modeling prior to experimental testing may be more efficient to achieving optimized flow fields. Also, experimentally diagnostic techniques for examining the localized current distributions within the porous electrode will be discussed later.

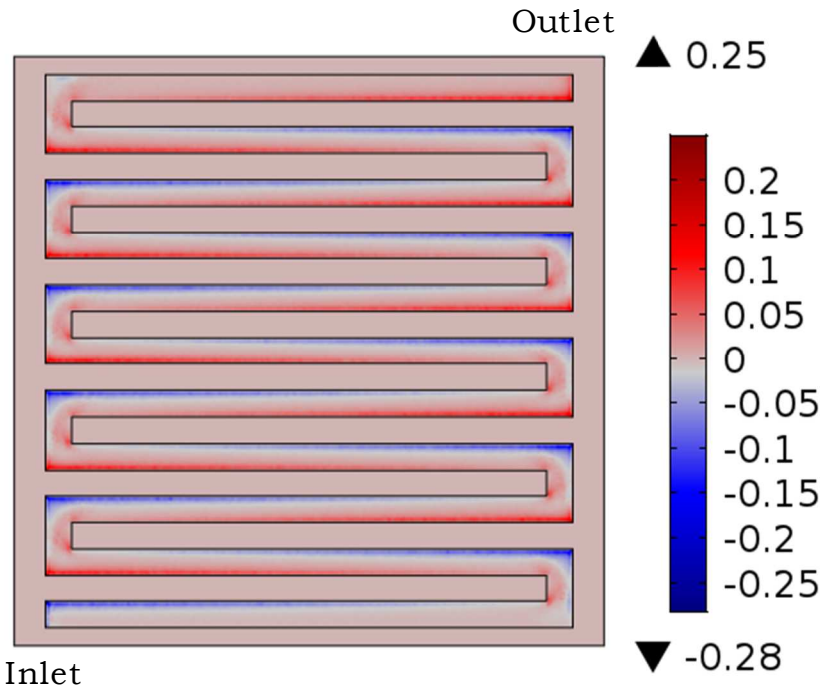

Figure 9 Flow penetrations at the interface between the flow field and porous electrode, SFF design. Reprinted with permission from ref. 103, Copyright 2018, Elsevier.

4. Large-scale flow battery stacks

To output larger cell voltage, power and capacity, large-scale flow batteries with multi-stack designs are required. Extra manifolds and channel ducts are necessary in large-scale flow battery stacks. Two examples of kW-scale flow battery stack systems presented in the literature are aqueous-based [183] and suspension-based [184]. The electroactive materials (anolyte and catholyte) are pumped through the manifold channels and connecting ports to the cell stacks. Increasing electrolyte volume stored in the external tanks and increased size of cell stacks (either cell number (voltage) or cell area (current)) will lead to larger power and energy. As an example, the power of an aqueous-based vanadium flow battery stack module reaches 15 kW when the number of cells is 120 (with an electrode area is 1,500 cm^2) under the nominal current density of

60 mA cm^{-2} and a single cell voltage of around 1.4 V [183]. To put this in perspective, such a stack built for a 1 MW installation would have roughly 67 modules and 8040 cells. Higher current density and/or cell area linearly scale the number of cells and modules for a given overall power. Both 5 kW and 10 kW vanadium flow battery stacks were also reported [185,186]. A prototype of a 5 kW vanadium flow battery stack under development by Pacific Northwest National Laboratory (PNNL) is shown in Fig. 10. Also, a commercial production of a 40 kW (225 W/L) vanadium flow battery stack developed by Vionx Energy Corporation is shown in Fig. 11. For the suspension-based lithium flow battery [184], the electroactive materials are both electronically and ionically conductive through the manifold and port channels. This is because the electroactive materials in the both anode and cathode have two phases: solid particles for electronic conductivity and liquid electrolyte for ionic conductivity. In designing large-scale flow battery stacks, flow distribution, pump loss and shunt current loss are three main factors to be considered. Trade-offs are to be made among achieving uniform flow distribution, minimizing pump and shunt current losses.

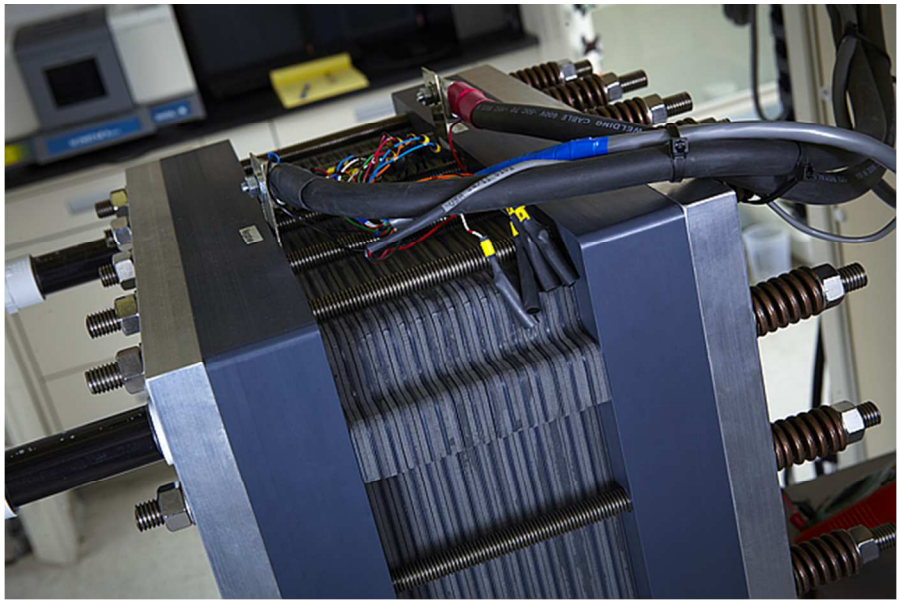

Figure 10 A photograph of a 5 kW vanadium flow battery stack under development in the laboratory. (Photo courtesy of Vince Sprenkle from Pacific Northwest National Laboratory).

Figure 11 A photograph of a 40 kW (225W/L) commercial vanadium flow battery stack production developed by Vionx Energy Corporation. (Photo courtesy of Vionx Energy Corporation and Michael L. Perry from United Technologies Research Center).

4.1 Optimization of non-uniform flow distributions

Uniformity of flow distributions is directly related to the utilization of electroactive materials through the porous electrode and consequently affects cell performance. Non-uniform flow distributions mean less amount of electrolyte is effectively utilized or less of the porous electrode surface is wet by the electrolyte and lead to loss in achievable power density, energy capacity and cell efficiencies. For a bad case, large "dead" zones (no reactant) of electrolyte occur within the porous electrode. These "dead" zones induced by the non-uniform flow distributions can be

simulated by the CFD technique. The goal of optimizing flow distributions by modeling is to achieve more uniform flow distributions to decrease the "dead" zones and increase the utilization of porous electrode, and consequently improve the electrochemical performance of flow batteries and stacks. Improved flow distribution through a single cell can be improved by cell design. Factors to be considered are flow channel width and depth, landing dimensions, porous electrode properties, such as permeability, wettability and thickness. Fluid properties are important which can be affected by composition and temperature. Also, fluid flow rate has a significant effect. From the aspect of electrochemistry, the electrolyte flow distributions also affect the ion concentration distributions and diffusion boundary layers associated with the mass transfer limiting current densities. Although the optimization of flow distributions is necessary for a small-scale flow battery [126], it is crucial for large-scale flow stack designs. An example of optimized flow distributions in a vanadium flow battery with 20 and 40-cell stack designs [187] are shown in Fig. 12, which indicates an optimized flow rate through each cell is approximately equal to the total entrance volumetric flow rate divided by the number of cells in the stack. The flow distributions as shown in Fig. 12 are rather uniform. But, it also can be seen that the uniformity of flow distributions at the center of cell stack is slightly better than the one at the ends of cell stack, and this is related to the "dead zones" that are more easily formed at the beginning and end of flowing through the stack. Both width and height of port channel leading from a common manifold to the individed cells can affect the flow distributions. Longer and narrower port channel results in more uniform flow distributions, but higher pressure drops. Also, a too high or too slow entrance flow rate may lead to seriously non-uniform cell-to-cell flow distributions.

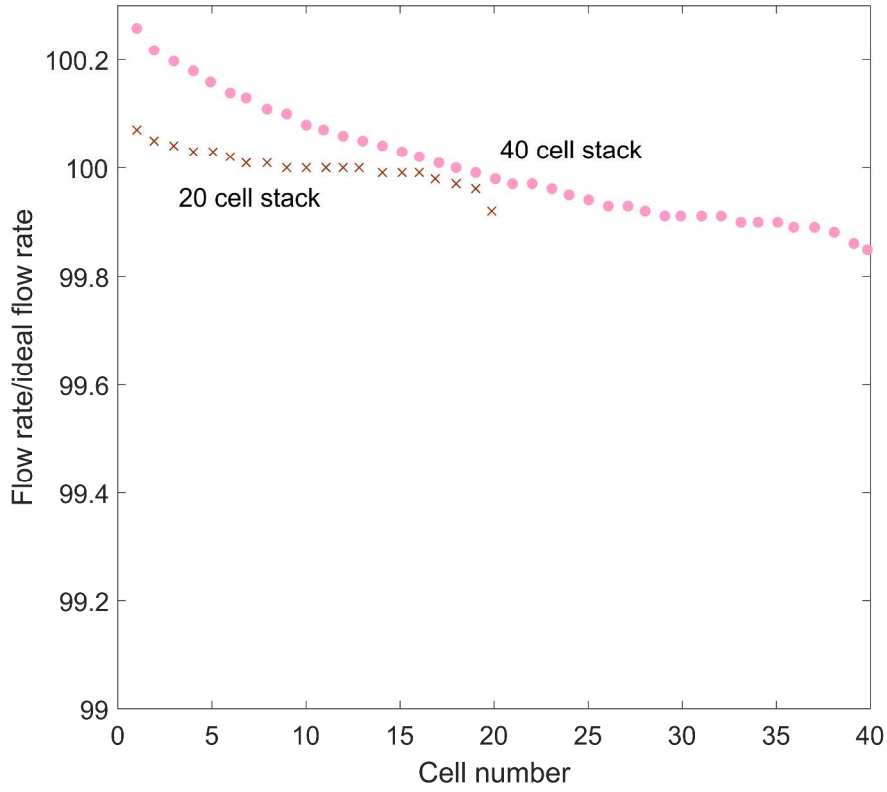

Figure 12 Flow distributions in the 20- and 40-cell vanadium flow stacks after optimization. Redrawn from ref. 187.

4.2 Shunt currents in bipolar cell stacks

Bipolar manifold stacks are required for large-scale flow batteries to realize higher output voltage and volumetric power density [183-187]. By this we mean cells are connected electrically in series with a bipolar plate (anode current collector on one side and cathode current collector on the other side). Cells are then fed electrolyte in parallel from a common manifold or plenum. However, extra "leakage" or "by-pass" or "shunt" currents [183,188] occur when a portion of the current passes through the manifold channels due to the presence of electrolyte, causing ion, or worse, electron conducting pathways. This results in losses of current and voltage efficiencies and power [189-191]. Research [192] also demonstrates that shunt currents may

have a relationship with corrosion and affect cell performance. To understand shunt currents, various models [193-201] have been developed. All of them use a resistance circuit network, which is based on the Kirchhoff's law. The earliest modeling work on shunt currents was reported by Katz et al. [193]. Later, Kaminski et al. [194] reported an equivalent circuit network model representing a *N* cell assembly as shown in Fig. 13 (a), which was first developed by Prokopius [202]. The conduction paths are symbolized by the resistor elements in both series and parallel among each other. A simpler solution algorithm [194] was developed to reduce the computational cost. An example as shown in Fig. 13 (b) and (c) was given to demonstrate the shunt current model. It can be seen that the maximum shunt current in the stack manifold

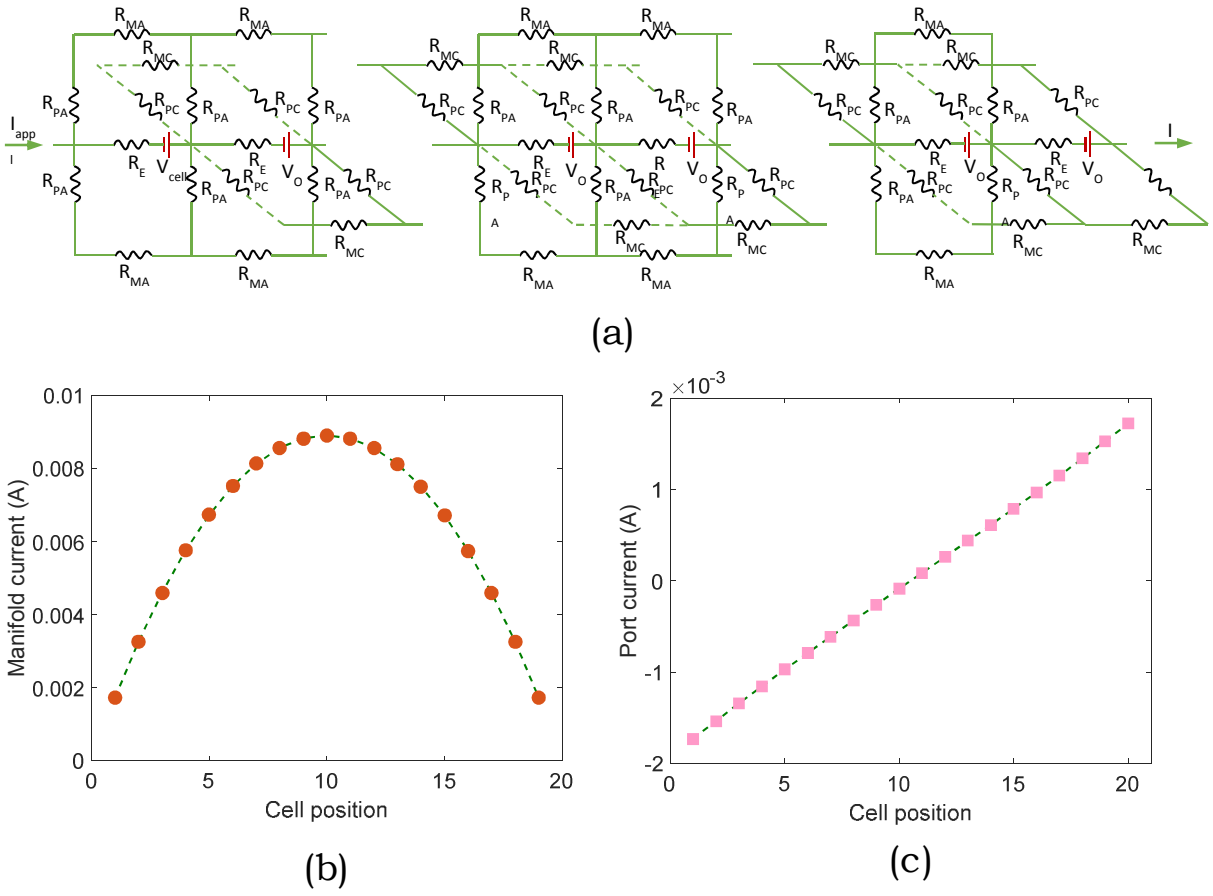

Figure 13 (a) Equivalent circuit model for shunt current. (b) and (c) A specific case of shunt current analysis, including manifold and port currents, using following assumed parameters: R_{PA}=5,000 Ω, R_{PC}=5,000 Ω, R_E=1 Ω,

I=0.5 A, R_{MA}=10 Ω, R_{MC}=5 Ω, V_{cell}=1.5 V and N=20, Where, R_{PA}: resistance of port channel at the anode side, R_{PC}: resistance of port channel at the cathode side, R_E: internal resistance, R_{MA}: resistance of manifold channel at the anode side, R_{MC}: resistance of manifold channel at the cathode side, I: applied current, V_{cell} is the cell potential and N is the number of flow cell. Redrawn from ref. 194.

occurs at the center cell in the stack (see Fig. 13 (b)). The port/leakage current increases from the center of the stack to the ends of the stack as shown in Fig. 13 (c). It seems that both distributions of manifold and port currents are symmetric with respect to the center cell of the stack. However, distributions of those currents may be not symmetric in other cases and should be related to the designs of the two-compartment (anode and cathode) cells. Shunt currents are affected by various factors including dimensions and layouts of manifold components, cell voltage, applied current, conductivity of electrolyte and number of cells in the stack. The electronic conductivity of electrode for slurry flow stacks also needs to be considered [203]. Minimizing the shunt currents is a goal for efficiency. One strategy for reducing shunt currents is to extend the path of electrolyte flow in the manifold and port channels, and consequently increase the electrical resistance and reduce shunt currents [147]. However, increasing the electrolyte flow path results in increased pressure drops, which increase the pumping losses. Therefore, minimization of shunt currents needs to take into account pumping losses and flow distributions for an optimal design.

4.3 Stack performance and commercialization

To date, few studies on design and performance of large-scale stack have been reported. Table 3 summarizes the details of size, efficiencies, power and energy achieved in vanadium flow battery stacks. The earliest work on flow battery stacks was reported by Skyllas-Kazacos et al. [13]. An output power of 1.33 kW was achieved in a 10-cell vanadium stack with an electrode

area of 1,500 cm^2 and an applied current density of 80 mA cm^{-2}. Zhao et al. [186] developed 10 kW-scale vanadium flow battery stacks by assembling 4 × 2 (serial × parallel) stacks, with each stack consisting of 14 cells. The electrode area and current density used in their work was 875 cm^2 and 85 mA cm^{-2}, respectively. In their system, they demonstrated a round-trip total stack electrical efficiency greater than 80 %. Recently, Pacific Northwest National Laboratory (PNNL) [111,187] developed a 1 kW vanadium flow battery stack by utilizing mixed electrolytes of hydrochloric acid and sulfuric acid. One main advantage of this mixed acid stack over the sulfate system is achieving a higher stack energy efficiency due to higher stable concentration of vanadium species in the mixed-acid electrolyte. This prototype of vanadium system was capable of delivering a power of 1.1 kW with an active electrode area of 780 cm^2 and applied current density of 80 mA cm^{-2}. Larger electrode area and more cells in the stacks were reported by Park et al. [204] and Wu et al. [185] for the vanadium stacks and power in the range of 5 kW ─ 10 kW. Flow battery stacks with high performance, i.e. high power and energy density, and high efficiencies and good stability, are still desired. It should be repeated that power density and current density are of primary importance in stack-type systems as these performance measures play a critical role in keeping stack cost low. Energy density, while important from a 'footprint' perspective, is less urgent for most RFB stationary storage installations. The 'balance of plant' components, especially tanks but also including pumps, filters and supporting electronics, dramatically exceed the stack in volume in most cases. Over past two decades, various patents [205-250] on flow fields, bipolar plates and stacks used in flow batteries have been issued and contribute to commercialization effects all over the world. Information on patents issued, inventors and countries is summarized in Table 4. For example, for the flow field designs, Perry et al. [224,231] filed patents for interleaved and interdigitated flow fields, which allow

electrolyte flow to be forced through the electrode and into adjacent flow channels. The electrolyte driven through the porous electrode enhances power density and efficiency. This reduces the capital costs, a critical need to foster commercialization of flow batteries.

Table 3 Summary of size, efficiencies, power and energy reported in vanadium RFBs with stack designs.

Number of flow cell	Electrode area (cm2)	Stack dimensions (L×W×H), mm	Applied current density (mA cm^{-2})	Performance						Year	References
				VE (%)	CE (%)	EE (%)	Power (kW)	Output voltage (V)	Energy (kWh)		
10	1,500	NA	80	73.2	98.2	71.9	1.33	NA	NA	1991	Skyllas-Kazacos, et al., [13]
14	875	440×340×200	70	89.7	87.1	78.1	1.14	18.7	NA	2006	Zhao et al., [186]
4×2 (serial × parallel) stacks, each stack is 14 cells	875	440×340×200	85	86.5	92.9	80.4	10.1	NA	NA	2006	Zhao et al., [186]
15	780	400×310×440	80/160	~ 86.3/~ 77.9	~ 95/~ 95	82/74	1.24/2.34	NA	1.4 – 1.5/1.3 – 1.4	2013	Kim et al., [187]
3	780	400×310×440	160/240	~ 85/~ 78	~ 95.2/~ 97.4	~ 81/~ 76	0.5/0.75	NA	NA	2016	Reed et al., [112]
31	2,714	622×660×657	60/90	82.2/77.0	92.4/90.8	76/70	6.2/8.9	NA	NA	2017	Park et al., [204]
40	1,800	NA	50/60/70/80	88.3/86.1/83.3/82.4	93.8/93.9/94.9/95.2	82.8/80.8/79.1/78.4	4.7/~ 5.5/~ 6.25/7.13	NA	NA	2017	Wu et al., [185]

Table 4 Summary of patents that have been applied or issued on flow fields, bipolar plates and stacks used in RFBs.

Patent title	Patent number	Country	Inventors	References
Redox flow battery system and cell stack	US6475661B1	United States	A. Pellegri and B.M. Broman	[205]
Method for operating redox flow battery and redox flow battery cell stack	US8221911B2	United States	T. Kumamoto and N. Tokuda	[206]
Cell stack for redox flow battery	US9017869B2	United States	H. Nakaishi, T. Kanno, S. Ogino, T. Ito, T. Shigematsu and N. Tokuda	[207]
Vanadium redox battery cell stack	US20070072067A1	United States	P. Symons, J. Genders and T.J. Hennessy	[208]
Cell frame for redox flow battery, and redox flow battery	US7670719B2	United States	H. Nakaishi, T. Kanno, S. Ogino, T. Ito, T. Shigematsu and N. Tokyda	[209]
Redox flow battery system for distributed energy storage	US8906529B2	United States	C.R. Horne, K. Kinoshita and D.B. Hickey	[210]
Multi voltage tap redox flow battery composed of stacked cell modules of adjustable cell area	WO2004079849A8	World Intellectual Property Organization	A. Zocchi, K. Kampanatsanyakorn and P.M. Spaziante	[211]
Common module stack component design	US20100136455A1	United States	R. Winter	[212]
Cell stack for a flowing electrolyte battery	US8293390B2	United States	A.R. Winter	[213]
Electrode frame and all-vanadium redox flow battery pile	CN101587959B	China	Z. Liu, H. Zhang, Y. Qiu and Y. Hao	[214]
Collector plate and bipolar collector plate, monocell and flow battery all including the same	CN202513235U	China	Z. Wan, Y. Fang, T. Li, C. Yin, H. Yang and G. Xie	[215]
Collecting plate of liquid flow battery and liquid flow battery	CN202127059U	China	Z. Wan, C. Yin, H. Tang, R. Wang, Y. Hu and G. Xie	[216]
Current collecting plate and the current collecting plate comprises a bipolar current collecting plate, and the cell flow cell	CN102623721B	China	H. Tang, C. Yin, T. Li, Z. Wan, Y. Fang and G. Xie	[217]
Frame for liquid flow battery electrode	CN102034993A	China	J. Xi, Z. Cao, R. Li, Z. Li, Z. Wu and J. Zhao	[218]
A flow cell with a bipolar plate or a monopolar plate structure and the all-vanaidum redox flow battery	CN104518222B	China	H. Zhang, Q. Zheng and F. Xing	[219]
Flow battery electrode common flow channel frame structure and a sealing method for sealing	CN105322196B	China	X. Ma, H. Zhang, X. Xu, Z. Yang, H. Jiang and S. Liu	[220]
Flow cell stack	US9269982B2	United States	S.K. Sahu, S. Kumar and S. Nair	[221]
Redox flow battery system with multiple independent stacks	US20130011704A1	United States	C.R. Horne, D.B. Hickey, O.K. Chang, S. Durairaj, R.J. Mosso and D. Bose	[222]
Frame of a cell of a redox flow battery	US8815428B2	United States	M. Harrer, H. Bucsich	[223]
Flow battery with interdigitated flow field	US9166243B2	United States	M.L. Perry	[224]
Electrode structure of vanadium redox flow battery	US8808897B2	United States	M.H. Liu, K.Y. Lee	[225]
Cascade redox flow battery systems	US8785023B2	United States	C.R. Horne, K. Kinoshita, D.B. Hickey, J.E. Sha and D. Bose	[226]

Flow battery with mixed flow	WO2013095378A1	World Intellectual Property Organization	R. Zhou, A. Pandy and M.L. Perry	[227]
Flow battery flow field having volume that is function of power parameter, time parameter and concentration parameter	EP2973827A4	European Patent Office	A. Smeltz, R.M. Darling, M.L. Perry and Z. Ding	[228]
Improved bipolar plate for flow batteries	WO2014109957A1	World Intellectual Property Organization	H. Xiao	[229]
Electrode assembly and flow battery with improved electrolyte distribution	WO201787365A1	World Intellectual Property Organization	A. Klassen and R. Blacker	[230]
Flow mixer with interleaved flow field	DK2514015T3	Denmark	M.L. Perry	[231]
Bipolar plate for redox flow battery	US20130037760A1	United States	S. Maeda, J. Sugawara and H. Hayami	[232]
Bipolar plate, redox flow battery and method for producing bipolar plate	US 20170047594A1	United States	K. Hanafusa, K. Itou, S. Okumura, T. Terao and H. Fujita	[233]
Cell frame for redox-flow cell and redox-flow cell	US20040202915A1	United States	H. Nakaishi, T. Kanno, S. Ogino, T. Ito, T. Shigematsu and N. Tokuda	[234]
Cell stack for flow cell	US9017869B2	United States	H. Nakaishi, T. Kanno, S. Ogino, T. Ito, T. Shigematsu and N. Tokuda	[235]
Bipolar, cell borders, cell stack and redox flow battery	DE202017106988U1	German	Sumitomo Electric Industries Ltd.	[236]
Frame body cell frame for a redox flow battery, and redox flow battery	DE212015000124U1	German	Sumitomo Electric Industries Ltd.	[237]
Cell frame, the cell stack, and redox flow battery	JP5831112B2	Japan	K. Yano, T. Shibata and T. Kumamoto	[238]
Cell frame structure for redox flow secondary cell, and manufacturing method therefor	JP2002246061A	Japan	K. Fujitani, N. Tokuda, T. Shinko and F. Katsumi	[239]
Cell frame for redox flow battery	JP2004335158A	Japan	Y. Kageyama, T. Kanno, N. Tokuda, K. Kino, T. Shinko and Y. Yoshiteru	[240]
And the redox flow battery cell frame	CN104282922B	China	S. Jing, M. Yan, T. Jing, T. He and Y. Fang	[241]
Cell stack and redox flow battery	WO2017010150A1	World Intellectual Property Organization	K. Kino, M. Kuwahara, T. Ito, F. Hayato, H. Kiyoaki, K. Moriuchi, S. Takasuke and H. Yamaguchi	[242]
Unified bipolar plate with flow frame for redox flow battery	KR101580405B1	Korea	K. Soo, C. Sunghwa	[243]
Bipolar plate, redox flow battery including the bipolar plate, and method of manufacture thereof	KR101751041B1	Korea	K. Soo, C. Sunghwa	[244]
Cell stack for a flowing electrolyte battery	US8293390B2	United States	A.R. Winter	[245]
Electrolyte flowing construction for electrolyte circulation-type cell stack secondary battery	US4732823A	United States	H. Ito, T. Hashimoto	[246]
Double pole plate for fluid flow battery	CN101325252B	China	S. Zhu, Q. Wang, B. Wang, J. Chen and F. Long	[247]
Bipolar plate frame and galvanic pile of flow battery	CN101847724B	China	B. Wang, Y. Fan, H. Han, D. Xu and X. Chen	[248]
Novel flow battery combined bipolar plate	CN201523039U	China	X. He and Z. Feng	[249]

Fluid flow battery galvanic pile structure for feeding liquid by using insulating plate and fluid flow battery comprising same	CN102136593A	China	H. Zhou, G. Zhang, J. Li, Z. Qin and K. Xue	[250]

5. Localized current distributions

To better understand physicochemical transport in RFBs, ex-situ and in-situ diagnostic techniques have been developed to examine the cell performance [251-254]. Although ex-situ approaches are capable of providing the averaged information, i.e. limiting current density, peak power density, discharge capacity and polarization curve, etc., the spatially-resolved details, such as concentration, potential and current distributions, are not easily detectable. In-situ techniques have been developed to obtain such localized information [255-263], and it is obviously beneficial to understanding key aspects for optimizing cell performance.

In particular, collecting the localized current distributions within the porous electrode is of major interest since current distributions reflect the utilizations of the electrode and the distributions of electrolyte reactants through the porous electrode. More uniform current distributions within the porous electrode reflect more consistent reaction rates across the electrode, leading to improved cell performance and even durability since 'hot spots' of high reaction rate and consequent heat generation are avoid. The localized current distributions within the porous electrode are affected by various factors: (1) properties of electrodes, i.e. thickness, porosity, permeability, active surface area and electronic conductivity, etc., (2) properties of electrolytes, i.e., concentration, viscosity, composition and ionic conductivity, etc., (3) kinetic reactions, i.e. kinetic rate constant, exchange current, etc., (4) electrolyte flow distributions, i.e. flow velocity and uniformity of flow distributions, etc., (5) flow field designs, i.e. layouts, dimensions, etc., and (5) operation conditions, i.e. entrance flow rate, state of charge, pH, working temperature and applied current/potential, etc.

Approaches to localized current measurement draw heavily from the approaches developed for fuel cell. Three main techniques for measuring current distributions have been reported in fuel

cell flow fields: (1) Hall-effect sensors [264,265], (2) shunt-resistors [266] and (3) printed circuit boards (PCB) [267,268]. The working principle of using Hall-effect sensors is to measure the localized magnetic intensity induced by an adjacent electric current field, and convert the localized magnetic intensity into the localized current indirectly. Both shunt-resistor and PCB techniques measure the localized voltage drop across the segments of a divided flow field, converting the voltage drop into the localized current by the Ohm's law directly. One main advantage of the PCB over the shunt-resistor technique is that the contact resistance between the segments and measurement system is lower [251,267,268]. As current versions of flow batteries with flow field designs, evolved from the fuel cell field, the techniques of measuring current distributions can be transplanted from fuel cells to flow batteries with flow fields. Early work [253] reported on measuring the localized current distributions in a vanadium flow battery with a specific flow field used the shunt-resistor technique: segmented gold-plated current collector (see Fig. 14 (a)) and a fully-segmented graphite flow field plate (see Fig. 14 (b)). The fully-segmented graphite flow field plate was superior because the 'smearing' of the information due to lateral spread of current was smaller.

Two more favorable characteristics for the PCB over the shunt-resistor approach were reported: higher spatial resolution and easier replacement. Clement et al. [251] used the PCB method to quantify the effects of various factors including flow rate, electrode properties, state of charge and applied current, on localized current distributions in a vanadium flow battery with a serpentine flow field design. Effects of segmented cell layout, i.e. partially and fully-segmented structures, flow rate and number of electrode layers, on current distributions in a vanadium flow battery with a serpentine flow field over the porous electrode were discussed. It was pointed out

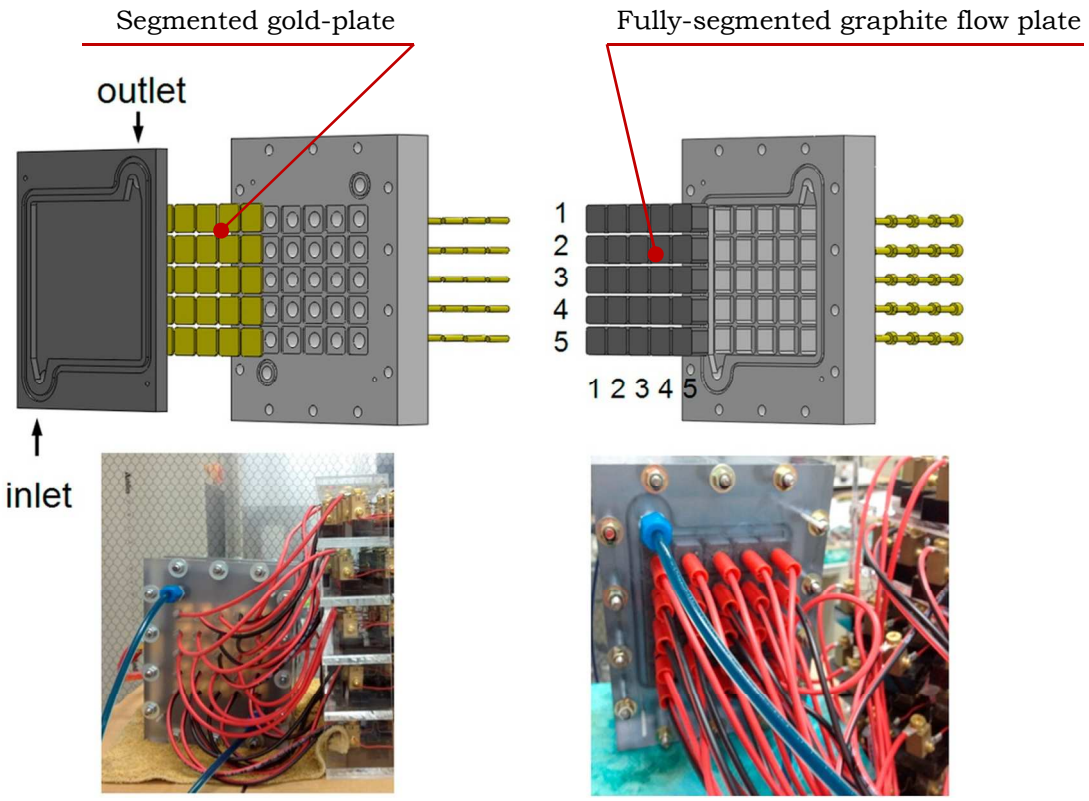

(a) Shunt-resistor approach

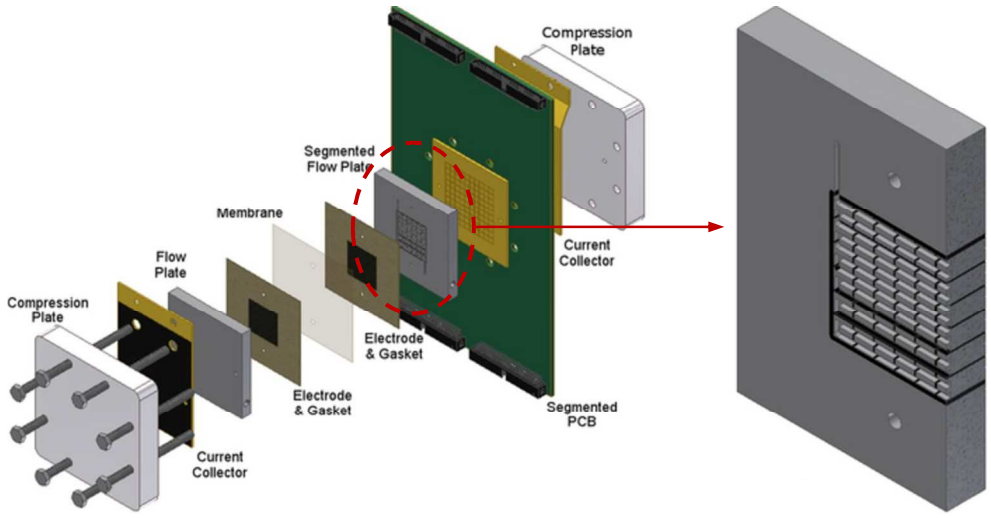

(b) Printed circuit boards (PCB) approach

Figure 14 Schematic diagram of shunt-resistor approach: (a) Segmented gold-plate current collector and fully-segmented graphite flow plate. Reprinted with permission from ref. 253, Copyright 2017,Elsevier. (b) Schematic

diagram of printed circuit boards (PCB) approach: PCB current distribution board and cross-section view of a fully-segmented flow plate. Reprinted with permission from ref. 251, Copyright 2016, The Electrochemical Society.

[251] that the fully-segmented design more effectively eliminates the spread of lateral current compared with a partially-segmented type. Lower flow rate and larger number of electrode layers result in less uniform current distributions in the porous electrode. Examinations of localized current distributions inform design changes that help to reduce the mass transfer over-potential, and improve utilization of materials and battery performance. Other studies [269-275] also used in-situ diagnostic techniques to examine localized potential distributions within the porous electrode. Compared with localized current distributions, localized potential distributions more indirectly relate to cell performance. Models predicting current distributions in RFBs with flow field designs are still in the early stages of development. Classical current distribution models for a porous electrode configuration [151,152] are not sufficient to capture the current distributions in RFBs with flow field designs and several new aspects should be considered. Forced convection is of importance for the three-dimensional (3D) flow fields of "flow-by" electrode configurations in order to supply reactants into the porous electrode. Time-dependent and finite kinetic processes also must be captured. Therefore, development of more advanced current distribution models for flow batteries with flow field designs is critical to advance the technology.

6. Limiting & maximum current densities

Limiting current density is significant criterion in evaluating the performance of electrochemical cells, including flow batteries, solid-state batteries, etc. Higher limiting current density, and the corollary higher operation current density at a given polarization leads to improved cell performance and consequently reduce capital costs. Several models predicting the limiting current density in an electrochemical cell have been developed. One classic model [2]

for estimating limiting current density is shown in Fig. 15 (a) and it is based on an assumption that the limiting current is completely controlled by the diffusion boundary layer formed at the interface between the porous electrode fiber and electrolyte. It is clear that this type of interfacial diffusion-limited current density is proportional to the specific surface area and thickness of the porous electrode, and inversely proportional to the thickness of the diffusion boundary layer. A thinner diffusion boundary layer yields a higher limiting current density. Both Darling et al. [95] and Wilson et al. [276] developed simplified models to roughly estimate the mass transfer coefficient for the laminar flow condition. Another model of explaining limiting current density as shown in Fig. 15 (b), was developed by Newman et al. [172]. The limiting current density was studied for the case of electrolyte flow through two parallel flat plates, with one plate being the electrode. Under this situation, it was assumed that electrolyte flow cannot penetrate into the electrode surface. This limiting current density is governed by the boundary layer formed between the electrolyte in the flow channel and the interface of the channel at the external electrode surface.

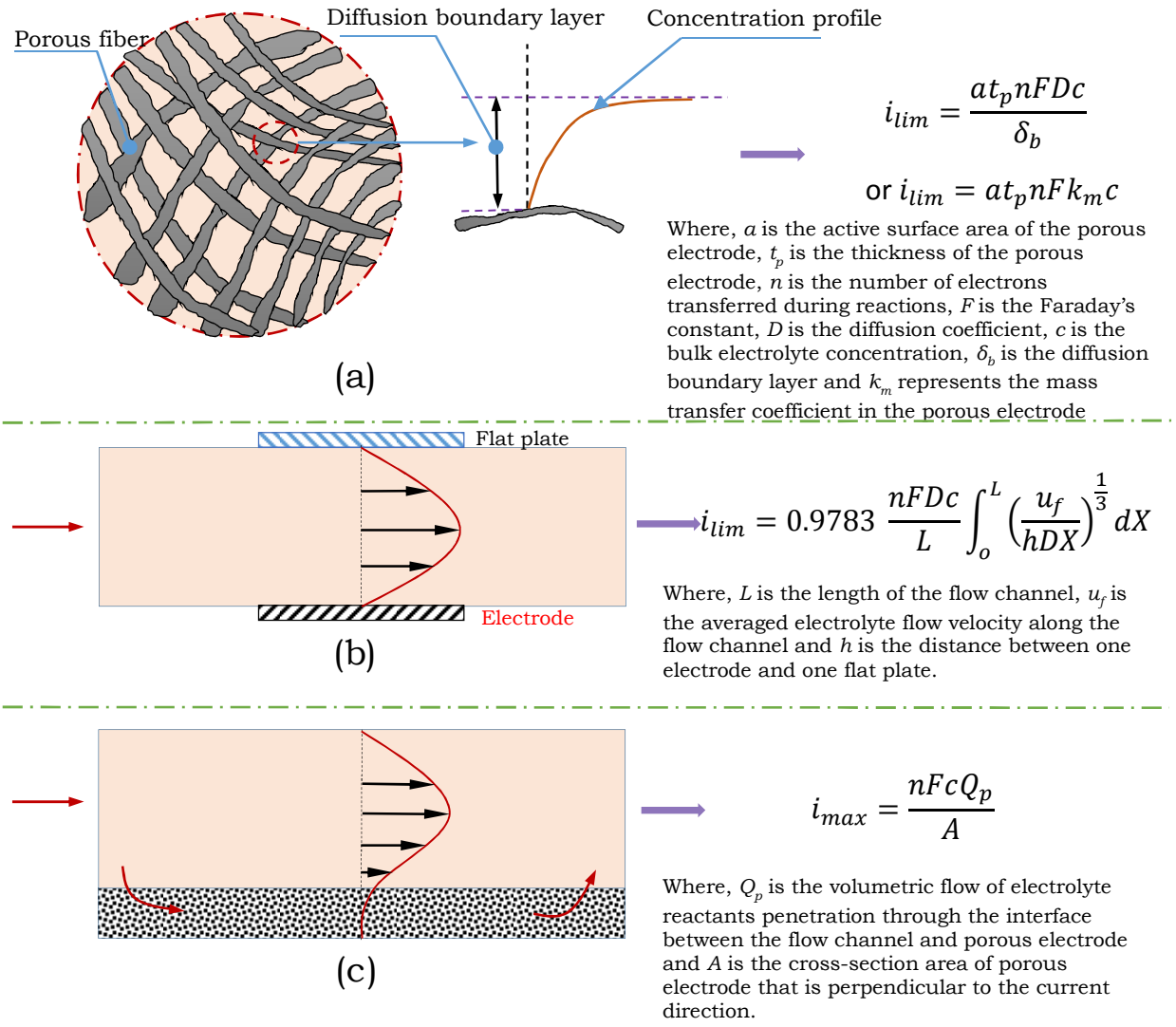

$$i_{lim} = \frac{at_p nFDc}{\delta_b}$$

or $i_{lim} = at_p nFk_m c$

Where, a is the active surface area of the porous electrode, t_p is the thickness of the porous electrode, n is the number of electrons transferred during reactions, F is the Faraday's constant, D is the diffusion coefficient, c is the bulk electrolyte concentration, δ_b is the diffusion boundary layer and k_m represents the mass transfer coefficient in the porous electrode

$$i_{lim} = 0.9783 \frac{nFDc}{L} \int_o^L \left(\frac{u_f}{hDX}\right)^{\frac{1}{3}} dX$$

Where, L is the length of the flow channel, u_f is the averaged electrolyte flow velocity along the flow channel and h is the distance between one electrode and one flat plate.

$$i_{max} = \frac{nFcQ_p}{A}$$

Where, Q_p is the volumetric flow of electrolyte reactants penetration through the interface between the flow channel and porous electrode and A is the cross-section area of porous electrode that is perpendicular to the current direction.

Figure 15 A diagram of three models on predicting the limiting and maximum current densities: (a) The case of current density limited by the diffusion boundary layer formed at the interface between the electrolyte reactants and porous fibers. (b) The case of current density limited by the diffusion boundary layer formed between one flat plate and one electrode, which does not allow electrolyte reactant penetration. (c) The case of current density limited by the stoichiometric availability of the electrolyte reactants penetrate through the porous electrode from the flow channel.

Recently, it has been found [103] that the limiting current density (order of magnitude of 3,000 mA cm^{-2}) estimated by the model described in Fig. 13 (a) significantly over-estimates while the

limiting current density (order of magnitude of 100 mA cm^{-2}) estimated by the model as shown in Fig. 15 (b) under-estimates the actual observed limiting current densities (an order of magnitude of 800 mA cm^{-2}, [90,94]) reported in a vanadium flow battery with a serpentine flow field over the porous carbon electrode with a typical experimental condition of 1M ion and 20 cm^3 min^{-1} entrance volumetric flow rate. It seems that the appearance of observed limiting current densities in a flow battery with a serpentine flow channel may not be governed by diffusion transport. Ke and Savinell et al. [99-103] concluded that the limiting current density achieved in a flow battery with a serpentine flow field over the porous electrode may be akin to the stoichiometric availability of reactant within the porous electrode instead of a diffusion control. This type of limiting current density controlled by the volumetric mass transfer through the porous electrode was called "maximum current density" as shown in Fig. 15 (c). This concept of maximum current density assumes that all of the electrolyte reactants penetration into the porous electrode from the serpentine flow field is consumed by the Faradaic reaction. The calculation of maximum current density is determined by the amount of electrolyte reactant penetration into the porous electrode. Various factors, i.e. initial entrance flow rate, dimensions and layouts of flow fields, thickness of porous electrode, and porosity and permeability of the porous electrode, etc., can affect the amount of flow penetration. It is worth noting that a much higher entrance flow rate will dramatically decrease the diffusion boundary layer and increase the amount of electrolyte flow penetration into the porous electrode, and consequently a much higher limiting or maximum current density can be achieved. Under a condition of a much higher entrance flow rate, the limiting current density predicted by the model described in Fig. 15 (a) will be much larger and the maximum current density predicted by the model described in Fig. 15 (c) will also be much larger. This may explain the observed limiting current density of

magnitude of 5,000 mA cm^{-2} reported by Elgammal and Zawodzinski et al. [169] measured at a very high entrance flow rate. The flow penetration is also strongly sensitive to the permeability of porous electrode, smaller permeability will leads to much less flow penetration and consequently much smaller maximum current density. When the active surface area of a porous electrode is small, then the limiting current density may actually be related to the kinetics and interfacial mass transfer factors instead of reactant availability within the porous electrode [103]. Nevertheless, kinetic limits are not taken into consideration among three models described in Fig. 15 (a)-(c) for estimating limiting current density. Thus, a more thorough analysis based on porous electrode theory by incorporating properties of porous electrode and electrolyte, i.e. electronic conductivity, ionic conductivity, kinetic rate constant, etc., would be useful. Examining localized current density distributions may further help to understand the role of kinetic limits. The maximum current density can be enhanced by driving all of the entrance electrolyte reactants from the flow fields through the porous electrode for RFBs with interdigitated flow field designs [95,116,118] and classic "flow-through" electrode configurations [155,157]. Nevertheless, increased ohmic losses, non-uniformity of flow distributions, and increased pressure drops/pumping losses, will be more important considerations for those designs in terms of cell performance.

Concluding remarks and perspective

Understanding of flow distributions, localized current distributions, limiting and maximum current densities will help to design better flow single cells. Understanding shunt currents and pressure distributions will help to design stacks to output larger power and more efficiently store energy for large-scale energy storage applications. To develop advanced flow batteries and stacks for high electrochemical performance, both experimental and modeling approaches are needed. Several main aspects to focus are in the near term include:

(1) Optimize electrolyte flow distributions to minimize non-uniformity, which can reduce the "dead zones" and increase the utilization of reactants. Achieving uniform flow distributions of electrolyte is especially important for the large-scale flow battery stack designs.

(2) Understand through theoretical analysis of localized potential and current distributions within the porous electrodes of RFBs. It is critical to develop new three-dimensional electrochemical models to fully capture the localized potential and current distributions within various electrode designs. Localized potential and current distributions within the porous electrode directly reflect the utilizations of electrolyte reactants and porous electrode. Understanding of them should be beneficial to the optimization of flow batteries.

(3) Explore novel flow field designs beyond current designs, i.e. serpentine and interdigitated, enabling high electrochemical performance. It is desired to reduce the polarization losses from kinetic, ohmic and mass transport limits in order to improve the performance and reduce the capital cost.

(4) Explore novel stack designs for high efficiency energy storage and power delivery. Long-term stability, low cost components, simple fabrication procedures, minimizing shunt currents and pumping losses are all desired to enhance commercialization success for grid applications.

Acknowledgements

This work was supported in-part under the "All-iron flow battery" project (grant number: DE-AR0000352) funded by Department of Energy (DOE) and by the Department of Energy, Office of Electricity Delivery and Energy Reliability of the United States (Dr. Imre Gyuk, Energy Storage Program). We appreciate the discussion with Prof. J. Adin Mann from Case Western Reserve University.

Nomenclature

a anode

A area (cm^2)

AR aspect ratio flow field

c cathode

C concentration (mol cm^{-3})

CFD computational fluid dynamics

CFF corrugated flow field

d diameter (cm)

D diffusion coefficient (cm^2 s^{-1})

EPL equal path length flow field

F Faraday's constant (96,485 C $equiv^{-1}$)

i current density (mA cm^{-2})

IFF interdigitated flow field

k_m mass transfer coefficient (cm s^{-1})

k permeability of porous electrode (m^2)

lim limiting

max maximum

n number of electron transferred

PFF parallel flow field

Q volumetric flow rate (cm^3 s^{-1})

R resistance (ohm)

sFF spiral flow field

SFF serpentine flow field

T-IFF tapered-interdigitated flow field

Greek symbols

ε porosity

δ thickness (cm)

Subscripts

appl applied

avg average

b boundary layer

ck Carman-Kozeny

f flow domain

in inlet

MA manifold channel at the anode side

MC manifold channel at the cathode side

o outlet

p porous domain

pf porous fiber

PA port channel at the anode side

PC port channel at the cathode side

References

1. T. Nguyen and R. F. Savinell, *Electrochem. Soc. Interface*, 2010, 54-56

2. A. Z. Weber, M. M. Mench, J. P. Meyers, P. N. Ross, J. T. Gostick and Q. Liu, *J. Appl. Electrochem.*, 2011, **41**, 1137-1164.

3. M. Skyllas-Kazacos, M. H. Chakrabarti, S. A. Hajimolana, F. S. Mjalli and M. Saleem, *J. Electrochem. Soc.*, 2011, **158**, R55-R779.

4. G. L. Soloveichik, *Chem. Rev.*, 2015, **115**, 11533-11588.

5. M. L. Perry and A. Z. Weber, *J. Electrochem. Soc.*, 2016, **163**, A5064-A5067.

6. B. Li and J. Liu, *Nat. Sci. Rev.*, 2017, **4**, 91-105.

7. Z. Yang, J. Zhang, M. C. Kintner-Meyer, X. Lu, D. Choi, J. P. Lemmon and J. Liu, *Chem. Rev.*, 2011, **111**, 3577-3613.

8. B. Dunn, H. Kamath and J. M. Tarascon, *Science*, 2011, **334**, 928-935.

9. S. Chu and A. Majumdar, *Nature*, 2012, **488**, 294-303.

10. H. Ibrahim and A. Ilinca, in *Energy Storage-Technologies and Applications*, ed. A. F. Zobaa, InTechOpen, 2013, ch. 1, pp. 1-40.

11. M. Rychcik and M. Skyllas-Kazacos, *J. Power Sources*, 1988, **22**, 59-67.

12. L. Li, S. Kim, W. Wang, M. Vijayakumar, Z. Xie, B. Chen, J. Zhang, G. Xia, J. Hu, G. Graff, J. Liu and Z. Yang, *Adv. Energy Mater.*, 2011, **1**, 394-400.

13. M. Skyllas-Kazacos, D. Kasherman, D. R. Hong and M. Kazacos, *J. Power Sources*, 1991, **35**, 399-404.

14. S. Roe, C. Menictas and M. Skyllas-Kazacos, *J. Electrochem. Soc.*, 2016, **163**, A5023-A5028.

15. M. Ulaganathan, V. Aravindan, Q. Yan, S. Madhavi, M. Skyllas-Kazacos and T. M. Lim, *Adv. Mater. Interfaces*, 2016, **3**, 1500309.

16. C. Fabjan, J. Garche, B. Harrer, L. Jorissen, C. Kolbeck, F. Philippi, G. Tomazic and F. Wagner, *Electrochim. Acta*, 2001, **47**, 825-831.

17. Q. Lai, H. Zhang, X. Li, L. Zhang and Y. Cheng, *J. Power Sources*, 2013, **235**, 1-4.

18. P. Singh and B. Jonshagen, *J. Power Sources*, 1991, **35**, 405-410.

19. J. H. Yang, H. S. Yang, H. W. Ra, J. Shim and J. D. Jeon, *J. Power Sources*, 2015, **275**, 294-297.

20. J. R. Zito, US Pat., 44 826 14A, 1984.

21. T. Sasaki, K. Tange, M. Okawa and Y. Suzuki, US Pat., 46 632 51A, 1987.

22. K. T. Cho, P. Ridgway, A. Z. Weber, S. Haussener, V. Battaglia and V. Srinivasan, *J. Electrochem. Soc.*, 2012, **159**, A1806-A1815.

23. G. Lin, P. Y. Chong, V. Yarlagadda, T. V. Nguyen, R. J. Wycisk, P. N. Pintauro, M. Bates, S. Mukerjee, M. C. Tucker and A. Z. Weber, *J. Electrochem. Soc.*, 2016, **163**, A5049-A5056.

24. L. W. Hruska and R. F. Savinell, *J. Electrochem. Soc.*, 1981, **128**, 18-25.

25. K. L. Hwathorne, J. S. Wainright and R. F. Savinell, *J. Electrochem. Soc.*, 2014, **161**, A1662-A1671.

26. K. L. Hawthorne, T. J. Petek, M. A. Miller, J. S. Wainright and R.F. Savinell, *J. Electrochem. Soc.*, 2015, **162**, A108-A113.

27. K. Gong, F. Xu, J. B. Grunewald, X. Ma, Y. Zhao, S. Gu and Y. Yan, *ACS Energy Lett.*, 2016, **1**, 89-93.

28. A. K. Manohar, K. M. Kim, E. Plichta, M. Hendrickson, S. Rawlings and S. R. Narayanan, *J. Electrochem. Soc.*, 2016, **163**, A5118-A5125.

29. M. C. Tucker, A. Phillips and A. Z. Weber, *ChemSusChem*, 2015, **8**, 3996-4004.

30. T. J. Petek, N. C. Hoyt, R. F. Savinell and J. S. Wainright, *J. Power Sources*, 2015, **294**, 620-626.

31. T. J. Petek, N. C. Hoyt, R. F. Savinell and J. S. Wainright, *J. Electrochem. Soc.*, 2016, **163**, A5001-A5009.

32. N. C. Hoyt, R. F. Savinell and J. S. Wainright, *Chem. Eng. Sci.*, 2016, **144**, 288-297.

33. M. Duduta, B. Ho, V. C. Wood, P. Limthongkul, V. E. Brunini, W. C. Carter and Y. M. Chiang, *Adv. Energy Mater.*, 2011, **1**, 511-516.

34. F. R. Brushett, J. T. Vaughey and A. N. Jansen, *Adv. Energy Mater.*, 2012, **2**, 1390-1396.

35. V. E. Brunini, Y. M. Chiang and W. C. Carter, *Electrochim. Acta*, 2012, **69**, 301-307.

36. Q. Huang, H. Li, M. Gratzel and Q. Wang, *Phys. Chem. Chem. Phys.*, 2013, **15**, 1793-1797.

37. Y. Yang, G. Zheng and Y. Cui, *Energy Environ. Sci.*, 2013, **6**, 1552-1558.

38. Y. Wang, P. He and H. Zhou, *Adv. Energy Mater.*, 2012, **2**, 770-779.

39. H. Chen, Q. Zou, Z. Liang, H. Liu, Q. Li and Y. Liu, *Nat. Commun.*, 2015, **6**, 5877.

40. C. Jia, F. Pan, Y. G. Zhu, Q. Huang, L. Lu and Q. Wang, *Sci. Adv.*, 2015, **1**, e1500886.

41. Z. Li, K. C. Smith, Y. Dong, N. Baram, F. Y. Fan, J. Xie, P. Limthongkul, W. C. Cater and Y. M. Chiang, *Phys. Chem. Chem. Phys.*, 2013, **15**, 15833-15839.

42. L. Sanz, D. Lloyd, E. Magdalena, J. Palma and K. Kontturi, *J. Power Sources*, 2014, **268**, 121-128.

43. D. Lloyd, T. Vainikka and K. Konturi, *Electrochim. Acta*, 2013, **100**, 18-23.

44. P. Peljo, D. Lloyd, N. Doan, M. Majaneva and K. Kontturi, *Phys. Chem. Chem. Phys.*, 2014, **16**, 2831-2835.

45. D. Lloyd, E. Magdalena, L. Sanz, L. Murtomaki and K. Kontturi, *J. Power Sources*, 2015, **292**, 87-94.

46. S. Schaltin, Y. Li, N. R. Brooks, J. Sniekers, I. F. J. Vankelecom, K. Binnemans and J. Fransaer, *Chem. Commun.*, 2016, **52**, 414-417.

47. B. Li, Z. Nie, M. Vijayakumar, G. Li, J. Liu, V. Sprenkle and W. Wang, *Nat. Commun.*, 2015, **6**, 6303.

48. B. Li, J. Liu, Z. Nie, W. Wang, D. Reed, J. Liu, P. McGrail and V. Sprenkle, *Nano Lett.*, 2016, **16**, 4335-4340.

49. Y. Zhao and H. R. Byon, *Adv. Energy Mater.*, 2013, **3**, 1630-1635.

50. M. Yu, W. D. McCulloch, D. R. Beauchamp, Z. Huang, X. Ren and Y. Wu, *J. Am. Chem. Soc.*, 2015, **137**, 8332-8335.

51. W. Wang, W. Xu, L. Cosimbescu, D. Choi, L. Li and Z. Yang, *Chem. Commun.*, 2012, **48**, 6669-6671.

52. B. Huskinson, M. P. Marshak, C. Suh, S. Er, M. R. Gerhardt, C. J. Galvin, X. Chen, A. Aspuru-Guzik, R. G. Gordon and M. J. Aziz, *Nature*, 2014, **505**, 195-198.

53. B. Yang, L. Hoober-Burkhardt, F. Wang, G. K. S. Prakash and S. R. Narayanan, *J. Electrochem. Soc.*, 2014, **161**, A1371-A1380.

54. B. Yang, L. Hoober-Burkhardt, S. Krishnamoorthy, A. Murali, G. K. S. Prakash and S. R. Narayanan, *J. Electrochem. Soc.*, 2016, **163**, A1442-A1449.

55. K. Lin, R. Gomez-Bombarelli, E. S. Beh, L. Tong, Q. Chen, A. Valle, A. Aspuru-Guzik, M. J. Aziz and R. G. Gordon*, Nat. Energy*, 2016, **1**, 16102.

56. E. S. Beh, D. D. Porcellinis, R. L. Gracia, K. T. Xia, R. G. Gordon and M. J. Aziz, *ACS Energy Lett.*, 2017, **2**, 639-644.

57. C. S. Sevov, D. P. Hickey, M. E. Cook, S. G. Robinson, S. Barnett, S. D. Minteer, M. S. Sigman and M. S. Sanford, *J. Am. Chem. Soc.*, 2017, **139**, 2924-2927.

58. W. Wang and V. Sprenkle, *Nat. Chem.*, 2016, **8**, 204-206.

59. B. Hu, C. DeBruler, Z. Rhodes and T. L. Liu, *J. Am. Chem. Soc.*, 2017, **139**, 1207-1214.

60. T. Janoschka, N. Martin, U. Martin, C. Friebe, S. Morgenstern, H. Hiller, M. D. Hager and U. S. Schubert, *Nature*, 2015, **527**, 78-81.

61. C. Stolze, C. Schmerbauch, C. Friebe and U. S. Schubert, *Energy Tech.*, 2017, **5**, 225-227.

62. J. Winsberg, T. Hagemann, S. Muench, C. Friebe, B. Haupler, T. Janoschka, S. Morgenstern, M. D. Hager and U. S. Schubert, *Chem. Mater.*, 2016, **28**, 3401-3405.

63. Y. Lu and J. B. Goodenough, *J. Mater. Chem.*, 2011, **21**, 10113-10117.

64. K. Lin, Q. Chen, M. R. Gerhardt, L. Tong, S. B. Kim, L. Eisenach, A. W. Valle, D. Hardee, R. G. Gordon, M. J. Aziz and M. P. Marshak, *Science*, 2015, **349**, 1529-1532.

65. N. Arroyo-Curras, J. W. Hall, J. E. Dick, R. A. Jones and A. J. Bard, *J. Electrochem. Soc.*, 2015, **162**, A378-A383.

66. A. Orita, M. G. Verde, M. Sakai and Y. S. Meng, *Nat. Commun.*, 2016, **7**, 13230.

67. P. K. Leung, C. Ponce de Leon, C. T. J. Low, A. A. Shah and F. C. Walsh, *J. Power Sources*, 2011, **196**, 5174-5185.

68. G. Nikiforidis, L. Berlouis, D. Hall and D. Hodgson, *Electrochim. Acta*, 2014, **115**, 621-629.

69. P. Liu, Y. Cao, G. Li, X. Gao, X. Ai and H. Yang, *ChemSusChem*, 2013, **6**, 802-806.

70. J. R. McKone and H. D. Abruna, US Pat., 2 017 017 955 8A1, 2017

71. M. Yu, W. D. McCulloch, D. R. Beauchamp, Z. Huang, X. Ren and Y. Wu, *J. Am. Chem. Soc.*, 2015, **137**, 8332-8335.

72. N. Yan, G. Li and X. Gao, *J. Mater. Chem. A*, 2013, **1**, 7012-7015.

73. K. Gong, Q. Fang, S. Gu, S. F. Y Li and Y. Yan, *Energy Environ. Sci.*, 2015, **8**, 3515-3530.

74. B. Hwang, M. S. Park and K. Kim, *ChemSusChem*, 2015, **8**, 310-314.

75. Y. Ding, Y. Zhao, Y. Li, J. B. Goodenough and G. Yu, *Energy Environ. Sci.*, 2017, **10**, 491-497.

76. P. J. Cappillino, H. D. Pratt III, N. S. Hudak, N. C. Tomson, T. M. Anderson and M. R. Anstey, *Adv. Energy Mater.*, 2014, **4**, 1300566.

77. B. Sun and M. Skyllas-Kazacos, *Electrochim. Acta*, 1992, **37**, 1253-1260.

78. L. Yue, W. Li, F. Sun, L. Zhao and L. Xing, *Carbon*, 2010, **48**, 3079-3090.

79. B. Li, M. Gu, Z. Nie, Y. Shao, Q. Luo, X. Wei, X. Li, J. Xiao, C. Wang, V. Sprenkle and W. Wang, *Nano Lett.*, 2103, **13**, 1330-1335.

80. M. Ulaganathan, A. Jain, V. Aravindan, S. Jayaraman, W. C. Ling, T. M. Lim, M. P. Srinivasan, Q. Yan and S. Madhavi, *J. Power Sources*, 2015, **274**, 846-850.

81. A. Bourke, M. A. Miller, R. P. Lynch, J. S. Wainright, R. F. Savinell and D. N. Buckley, *J. Electrochem. Soc.*, 2015, **162**, A1547-A1555.

82. T. M. Tseng, R. H. Huang, C. Y. Huang, C. C. Liu, K. L. Hsueh and F. S. Shieu, *J. Electrochem. Soc.*, 2014, **161**, A1132-A1138.

83. A. M. Pezeshki, J. T. Clement, G. M. Veith, T. A. Zawodzinski and M. M. Mench, *J. Power Sources*, 2015, **294**, 333-338.

84. W. Dai, L. Yu, Z. Li, J. Yan, L. Liu, J. Xi and X. Qiu, *Electrochim. Acta*, 2014, **132**, 200-207.

85. L. Cao, Q. Sun, Y. Gao, L. Liu and H. Shi, *Electrochim. Acta*, 2015, **158**, 24-34.

86. T. Luo, O. David, Y. Gendel and M. Wessling, *J. Power Sources*, 2016, **312**, 45-54.

87. J. Kim, J. D. Jeon and S. Y. Kwak, *Electrochem. Commun.*, 2014, **38**, 68-70.

88 X. Teng, C. Sun, J. Dai, H. Liu, J. Su and F. Li, *Electrochim. Acta*, 2013, **88**, 725-734.

89. W. Dai, Y. Shen, Z. Li, L. Yu, J. Xi and X. Qiu, *J. Mater. Chem. A*, 2014, **2**, 12423-12432.

90. D. S. Aaron, Q. Liu, Z. Tang, G. M. Grim, A. B. Papandrew, A. Turhan and T. A. Zawodzinski, *J. Power Sources*, 2012, **206**, 450-453.

91. Q. Liu, G. M. Grim, A. B. Papandrew, A. Turban, T. A. Zawodzinski and M. M. Mench, *J. Electrochem. Soc.*, 2012, **159**, A1246-A1252.

92. Q. Xu, T. Zhao and P. Leung, *Appl. Energy*, 2013, **105**, 47-56.

93. M. L. Perry, R. M. Darling and R. Zaffou, *ECS Trans.*, 2013, **53**, 7-16.

94. I. Mayrhuber, C. R. Dennison, V. Kalra and E. C. Kumbur, *J. Power Sources*, 2014, **260**, 251-258.

95. R. M. Darling and M. L. Perry, *J. Electrochem. Soc.*, 2014, **161**, A1381-A1387.

96. T. J. Latha and S. Jayanti, *J. Power Sources*, 2014, **248**, 140-146.

97. T. J. Latha and S. Jayanti, *J. Appl. Electrochem.*, 2014, **44**, 995-1006.

98. S. Kumar and S. Jayanti, *J. Power Sources*, 2016, **307**, 782-787.

99. X. Ke, MS thesis, Case Western Reserve University, 2014.

100. X. Ke, J. I. D. Alexander, J. M. Prahl and R. F. Savinell, *J. Power Sources*, 2014, **270**, 646-657.

101. X. Ke, J. I. D. Alexander, J. M. Prahl and R. F. Savinell, *J. Power Sources*, 2015, **288**, 308-313.

102. X. Ke, J. M. Prahl, J. I. D. Alexander and R. F. Savinell, *Electrochim. Acta*, 2017, **223**, 124-134.

103. X. Ke, J. M. Prahl, J. I. D. Alexander and R. F. Savinell, *J. Power Sources*, 2018, **384**, 295-302.

104. C. R. Dennison, E. Agar, B. Akuzum and E. C. Kumbur, *J. Electrochem. Soc.*, 2016, **163**, A5163-A5169.

105. J. Houser, J. Clement, A. Pezeshki and M. M. Mench, *J. Power Sources*, 2016, **302**, 369-377.

106. J. Houser, A. Pezeshki, J. T. Clement, D. S. Aaron and M. M. Mench, *J. Power Sources*, 2017, **351**, 96-105.

107. A. M. Pezeshi, R. L. Sacci, F. M. Delnick, D. S. Aaron and M. M. Mench, *Electrochim. Acta*, 2017, **229**, 261-270.

108. K. M. Lisboa, J. Marschewski, N. Ebejer, P. Ruch, R. M. Cotta, B. Michel and D. Poulikakos, *J. Power Sources*, 2017, **359**, 322-331.

109. J. Marschewski, L. Brenner, N. Ebejer, P. Ruch, B. Michel and D. Poulikakos, *Energy Environ. Sci.*, 2017, **10**, 780-787.

110. K. Cho, P. Ridgway, A. Z. Weber, S. Haussener, V. Battaglia and V. Srinivasan, *J. Electrochem. Soc.*, 2012, **159**, A1806-A1815.

111. D. Reed, E. Thomsen, B. Li, W. Wang, Z. Nie, B. Koeppel and V. Sprenkle, *J. Power Sources*, 2016, **306**, 24-31.

112. A. Bhattarai, N. Wai, R. Schweiss, A. Whitehead, T. M. Lim and H. H. Hng, *J. Power Sources*, 2017, **341**, 83-90.

113. Y. Zeng, X. Zhou, L. An, L. Wei and T. Zhao, *J. Power Sources*, 2016, **324**, 738-744.

114. Y. Zeng, X. Zhou, L. Zeng, X. Han and T. Zhao, *J. Power Sources*, 2016, **327**, 258-264.

115. Q. Zheng, F. Xing, X. Li, G. Ning and H. Zhang, *J. Power Sources*, 2016, **324**, 402-411.

116. X. You, Q. Ye and P. Cheng, *Int. Commun. Heat Mass Transf.*, 2016, **75**, 7-12.

117. Q. Xu, T. Zhao and C. Zhang, *Electrochim. Acta*, 2014, **142**, 61-67.

118. R. J. Kee and H. Zhu, *J. Power Sources*, 2015, **299**, 509-518.

119. E. Knudsen, P. Albertus, K. T. Cho, A. Z. Weber and A. Kojic, *J. Power Sources*, 2015, **299**, 617-628.

120. S. Rudolph, U. Schroder, R. I. Bayanov, K. Blenke and I. M. Bayanov, *J. Electroanal. Chem.*, 2015, **736**, 117-126.

121. J. Choe, J. Kim and D. G. Lee, *Compos. Struct.*, 2016, **158**, 333-339.

122. Z. Wei, J. Zhao, M. Skyllas-Kazacos and B. Xiong, *J. Power Sources*, 2014, **260**, 89-99.

123. S. Ressel, A. Laube, S. Fischer, A. Chica, T. Flower and T. Struckmann, *J. Power Sources*, 2017, **355**, 199-205.

124. M. C. Tucker, A. Weiss and A. Z. Weber, *J. Power Sources*, 2016, **327**, 591-598.

125. P. Leung, M. R. Mohamed, A. A. Shah, Q. Xu and M. B. Conde-Duran, *J. Power Sources*, 2015, **274**, 651-658.

126. J. Escudero-Gonzalez and P. A. Lopez-Jimenez, *J. Power Sources*, 2014, 251, 243-253.

127. K. T. Cho, P. Albertus, V. Battaglia, A. Kojic, V. Srinivasan and A. Z. Weber, *Energy Tech.*, 2013, **1**, 596-608.

128. Q. Zheng, F. Xing, X. Li, T. Liu, Q. Lai, G. Ning and H. Zhang, *J. Power Sources*, 2015, **277**, 104-109.

129. A. Tang, J. Bao and M. Skyllas-Kazacos, *J. Power Sources*, 2014, **248**, 154-162.

130. X. Ma, H. Zhang, C. Sun, Y. Zhou and T. Zhang, *J. Power Sources*, 2012, **203**, 153-158.

131. J. Chen, B. Wang and H. Lv, *Adv. Mater. Res.*, 2011, **236-238**, 604-607.

132. K. Oh, T. Kang, S. Park, M. C. Tucker, A. Z. Weber and H. Ju, *Electrochim. Acta*, 2017, **230**, 160-173.

133. J. D. Milshtein, K. M. Tenny, J. L. Barton, J. Drake, R. M. Darling and F. R. Brushett, *J. Electrochem. Soc.*, 2017, **164**, E3265-E3275.

134. Y. Cheng, H. Zhang, Q. Lai, X. Li and D. Shi, *Electrochim. Acta*, 2013, **105**, 628-621.

135. X. Li and I. Sabir, *Int. J. Hydrogen Energy*, 2005, **30**, 359-371.

136. A. Kumar and R. G. Reddy, *J. Power Sources*, 2003, **113**, 11-18.

137. V. Mehta and J. S. Cooper, *J. Power Sources*, 2003, **114**, 32-53.

138. A. Z. Weber and J. Newman, *Chem. Rev.*, 2004, **104**, 4679-4726.

139. C. Wang, *Chem. Rev.*, 2004, **104**, 4727-4766.

140. W. Wang, Q. Luo, B. Li, X. Wei, L. Li and Z. Yang, *Adv. Funct. Mater.*, 2013, **23**, 970-986.

141. S. Shin, S. Yun and S. Moon, *RSC Adv.*, 2013, **3**, 9095-9116.

142. C. Ding, H. Zhang, X. Li, T. Liu and F. Xing, *J. Phys. Chem. Lett.*, 2013, **4**, 1281-1294.

143. P. Leung, A. A Shah, L. Sanz, C. Flox, J. R. Morante, Q. Xu, M. R. Mohamed, C. Ponce de Leon and F. C. Walsh, *J. Power Sources*, 2017, **360**, 243-283.

144. Y. Huang, S. Gu, Y. Yan and S. Li, *Curr. Opin. Chem. Eng.*, 2015, **8**, 105-113.

145. M. H. Chakrabarti, N. P. Brandon, S. A. Hajimolana, F. Tariq, V. Yufit, M. A. Hashim, M. A. Hussain, C. T. J. Low and P. V. Aravind, *J. Power Sources*, 2014, **253**, 150-166.

146. J. A. Kowalski, L. Su, J. D. Milshtein and F.R. Brushett, *Curr. Opin. Chem. Eng.*, 2016, **13**, 45-52.

147. L. F. Arenas, C. Ponce de Leon and F. C. Walsh, J. Energy Storage, 2017, **11**, 119-153.

148. B. R. Chalamala, T. Soundappan, G. R. Fisher, M. R. Anstey, V. V. Viswanathan and M. L. Perry, Proc. IEEE, 2014, **102**, 1-24.

149. X. Zhou, T. Zhao, L. An, Y. Zeng and L. Wei, *J. Power Sources*, 2017, 339: 1-12.

150. Q. Xu, T. Zhao, *Transport and Electrochemical Characteristics in Flow Batteries*, LAMBERT Academic Publishing, Saarbrücken, 2017.

151. J. S. Newman and C. W. Tobias, *J. Electrochem. Soc.*, 1962, **109**, 1183-1191.

152. J. S. Newman and W. Tiedemann, *AlChE J.*, 1975, **21**, 25-41.

153. S. Langlois and F. Coeuret, *J. Appl. Electrochem.*, 1990, **20**, 740-748.

154. K. Kinoshita and S. C. Leach, *J. Electrochem. Soc.*, 1982, **129**, 1993-1997.

155. K. W. Knehr, E. Agar, C. R. Dennison, A. R. Kalidindi and E. C. Kumbur, *J. Electrochem. Soc.*, 2012, **159**, A1446-A1459.

156. A. A. Shah, R. Tangirala, R. Singh, R. G. A. Wills and F. C. Walsh, *J. Electrochem. Soc.*, 2011, **158**, A671-A677.

157. A. A. Shah, M. J. Watt-Smith and F.C. Walsh, *Electrochim. Acta*, 2008, **53**, 8087-8100.

158. H. Al-Fetlawi, A. A. Shah and F. C. Walsh, *Electrochim. Acta*, 2009, **55**, 78-89.

159. A. A. Shah, H. Al-Fetlawi and F. C. Walsh, *Electrochim. Acta*, 2010, **55**, 1125-1139.

160. H. Al-Fetlawi, A. A. Shah and F. C. Walsh, *Electrochim. Acta*, 2010, **55**, 3192-3205.

161. D. Krishnamurthy, E. O. Johansson, J. W. Lee and E. Kjeang, *J. Power Sources*, 2011, **196**, 10019-10031.

162. K. S. Salloum and J. D. Posne, *J. Power Sources*, 2010, **195**, 6941-6944.

163. S. Moore, D. Sinton and D. Erickson, *J. Power Sources*, 2011, **196**, 9481-9487.

164. J. W. Lee, PhD thesis, Simon Fraser University, 2012.

165. E. Kjeang, N. Djilali and D. Sinton, *J. Power Sources*, 2009, **186**, 353-369.

166. J. A. Trainham, J. S. Newman, *Electrochim. Acta*, 1981, **26**, 455-469.

167. P. S. Fedkiw, *J. Electrochem. Soc.*, 1981, **128**, 831-838.

168. X. You, Q. Ye, T. V. Nguyen and P. Cheng, *J. Electrochem. Soc.*, 2016, **163**, A447-A457.

169. R. A. Elgammal, Z. Tang, C. N. Sun, J. Lawton and T. A. Zawodzinski, *Electrochim. Acta*, 2017, **237**, 1-11.

170. R. B. Bird, W. E. Stewart and E. N. Lightfoot, *Transport Phenomena*, John Wiley & Sons, Inc., New York, 2007

171. G. Neale and W. Nader, Can. J. Chem. Eng., 1974, **52**, 475-478.

172. J. S. Newman and K. E. Thomas-Alyea, *Electrochemical Systems*, John Wiley & Sons, Inc., New York, 2004

173. A. Tamayol, F. McGregor and M. Bahrami, *J. Power Sources*, 2012, **204**, 94-99.

174. M. A. Van Doormaal and J. G. Pharoah, *Int. J. Numer. Method Fluids*, 2009, **59**, 75-89.

175. J. T. Gostick, M. W. Fowler, M. D. Pritzker, M. A. Ioannidis and L. M. Behra, *J. Power Sources*, 2006, **162**, 228-238.

176. I. S. Hussaini and C. Y. Wang, *J. Power Sources*, 2010, **195**, 3830-3840.

177. P. C. Carman, *Trans. Inst. Chem. Eng. (London)*, 1937, **15**, 150-166.

178. J. Kozeny, Stizungsber Akad. Wiss. Wien, 1927, **136**, 271-306.

179. M. M. Tomadakis, *J. Compos. Mater.*, 2005, **39**, 163-188.

180. R. Carta, S. Palmas, A. M. Polcaro and G. Tola, *J. Appl. Electrochem.*, 1991, **21**, 793-798.

181. S. Brunauer, P. H. Emmett and E. Teller, *J. Chem. Soc.*, 1938, **60**, 309-319.

182. G. Fagerlund, *Mater. Struct.*, 1973, **6**, 239-245.

183. Q, Ye, J. Hu, P. Cheng and Z. Ma, *J. Power Sources*, 2015, **296**, 352-364.

184. K. C. Smith, V. E. Brunini, Y. Dong, Y. M. Chiang and W. C. Carter, *Electrochim. Acta*, 2014, **147**, 460-469.

185. X. Wu, X. Yuan, Z. Wang, J. Liu, Y. Hu, Q. Deng, X. Yin, Q. Zhou, W. Zhou and Y. Wu, *J. Solid State Electrochem.*, 2017, **21**, 429-435.

186. P. Zhao, H. Zhang, H. Zhou, J. Chen, S. Gao and B. Yi, *J. Power Sources*, 2006, **162**, 1416-1420.

187. S. Kim, E. Thomsen, G. Xia, Z. Nie, J. Bao, K. Recknagle, W. Wang, V. Viswanathan, Q. Luo, X. Wei, A. Crawford, G. Coffey, G. Maupin and V. Sprenkle, *J. Power Sources*, 2013, **237**, 300-309.

188. A. T. Kuhn and J. S. Booth, *J. Appl. Electrochem.*, 1980, **10**, 233-237.

189. A. Tang, J. McCann, J. Bao and M. Skyllas-Kazacos, *J. Power Sources*, 2013, **242**, 349-356.

190. F. Xing, H. Zhang and X. Ma, *J. Power Sources*, 2011, **196**, 10753-10757.

191. H. Fink and M. Remy, *J. Power Sources*, 2015, **284**, 547-553.

192. R. M. Darling, H. Shiau, A. Z. Weber and M. L. Perry, *J. Electrochem. Soc.*, 2017, **164**, E3081-E3091.

193. M. Katz, *J. Electrochem. Soc.*, 1978, **125**, 515-520.

194. E. A Kaminski and R. F. Savinell, *J. Electrochem. Soc.*, 1983, **130**, 1103-1107.

195. R. E. White, C. W. Walton, H. S. Burney and R. N. Beaver, *J. Electrochem. Soc.*, 1986, **133**, 485-492.

196. M. Z. Yang, H. Wu and J. R. Selman, *J. Appl. Electrochem.*, 1989, **19**, 247-254.

197. C. Comninellis, E. Plattner and P. Bolomey, *J. Appl. Electrochem.*, 1991, **21**, 415-418.

198. E. R. Henquin and J. M. Bisang, *J. Appl. Electrochem.*, 2005, **35**, 1183-1190.

199. F. T. Wandschneider, S. Rohm, P. Fischer, K. Pinkwart, J. Tubke and H. Nirschl, *J. Power Sources*, 2014, **261**, 64-74.

200. Y. S. Chen, S. Y. Ho, H. W. Chou and H. J. Wei, *J. Power Sources*, 2018, **390**, 168-175.

201. S. Konig, M. R. Suriyah and T. Leibfried, *J. Power Sources*, 2015, **281**, 272-284.

202. P. R. Prokopius, Model for Calculating Electrolytic Shunt Path Losses in Large Electrochemical Conversion Systems, NASA-TM-X-3359, Technical Report, 76N21702, 1976,

https://ntrs.nasa.gov/archive/nasa/casi.ntrs.nasa.gov/19760014614.pdf, (accessed September 2018).

203. X. Ke, J. S. Wainright and R. F. Savinell, presented in part at the 232nd ECS Meeting, National Harbor, Washington DC, October, 2017

204. D. J. Park, K. S. Jeon, C. H. Ryu and G. J. Hwang, *J. Ind. Eng. Chem.*, 2017, **45**, 387-390.

205. A. Pellegri and B. M. Broman, US Pat., 647 566 1B1, 2002

206. T. Kumamoto and N. Tokuda, US Pat., 822 191 1B2, 2012.

207. H. Nakaishi, T. Kanno, S. Ogino, T. Ito, T. Shigematsu and N. Tokuda, US Pat., 901 786 9B2, 2015.

208. P. Symons, J. Genders and T. J. Hennessy, US Pat., 2007 007 206 7A1, 2007.

209. H. Nakaishi, T. Kanno, S. Ogino, T. Ito, T. Shigematsu and N. Tokyda, US Pat., 767 071 9B2, 2010.

210. C. R. Horne, K. Kinoshita and D. B. Hickey, US Pat., 890 652 9B2, 2014.

211. A. Zocchi, K. Kampanatsanyakorn and P. M. Spaziante, WO Pat., 200 407 984 9A8, 2005

212. R. Winter, US Pat., 2 010 013 645 5A1, 2010.

213. A. R. Winter, US Pat., 829 339 0B2, 2012.

214. Z. Liu, H. Zhang, Y. Qiu and Y. Hao, CN Pat., 1 015 879 59B, 2012.

215. Z. Wan, Y. Fang, T. Li, C. Yin, H. Yang and G. Xie, CN Pat., 2 025 132 35U, 2012.

216. Z. Wan, C. Yin, H. Tang, R. Wang, Y. Hu and G. Xie, CN Pat., 2 021 270 59U, 2012.

217. H. Tang, C. Yin, T. Li, Z. Wan, Y. Fang and G. Xie, CN Pat., 1 026 237 21B, 2012.

218. J. Xi, Z. Cao, R. Li, Z. Li, Z. Wu and J. Zhao, CN Pat., 1 020 349 93A, 2011.

219. H. Zhang, Q. Zheng and F. Xing, CN Pat., 1 045 182 22B, 2017.

220. X. Ma, H. Zhang, X. Xu, Z. Yang, H. Jiang and S. Liu, CN Pat., 1 053 221 96B, 2018.

221. S. K. Sahu, S. Kumar and S. Nair, US Pat., 926 998 2B2, 2016.

222. C. R. Horne, D. B. Hickey, O. K. Chang, S. Durairaj, R. J. Mosso and D. Bose, US Pat., 2 013 001 170 4A1, 2013

223. M. Harrer and H. Bucsich, US Pat., 8815428B2, 2014.

224. M. L. Perry, US Pat., 916 624 3B2, 2015.

225. M. H. Liu and K. Y. Lee, US Pat., 8808897B2, 2014.

226. C. R. Horne, K. Kinoshita, D. B. Hickey, J. E. Sha and D. Bose, US Pat., 878 502 3B2, 2014.

227. R. Zhou, A. Pandy and M. L. Perry, WO Pat., 201 309 537 8A1, 2013.

228. A. Smeltz, R. M. Darling, M. L. Perry and Z. Ding, EP Pat., 297 382 7A4, 2016.

229. H. Xiao, WO Pat., 201 410 995 7A1, 2014.

230. A. Klassen and R. Blacker, WO Pat., 201 708 736 5A1, 2017.

231. M. L. Perry, DK Pat., 251 401 5T3, 2015.

232. S. Maeda, J. Sugawara and H. Hayami, US Pat., 2 013 003 776 0A1, 2013.

233. K. Hanafusa, K. Itou, S. Okumura, T. Terao and H. Fujita, US Pat., 2 017 004 759 4A1, 2017.

234. H. Nakaishi, T. Kanno, S. Ogino, T. Ito, T. Shigematsu and N. Tokuda, US Pat., 2 004 020 291 5A1, 2004.

235. H. Nakaishi, T. Kanno, S. Ogino, T. Ito, T. Shigematsu and N. Tokuda, US Pat., 901 786 9B2, 2015.

236. Sumitomo Electric Industries Ltd., DE Pat., 20 201 710 698 8U1, 2017.

237. Sumitomo Electric Industries Ltd., DE Pat., 21 201 500 012 4U1, 2016.

238. K. Yano, T. Shibata and T. Kumamoto, JP Pat., 583 111 2B2, 2015.

239. K. Fujitani, N. Tokuda, T. Shinko and F. Katsumi, JP Pat., 20 022 460 61A, 2002.

240. Y. Kageyama, T. Kanno, N. Tokuda, K. Kino, T. Shinko and Y. Yoshiteru, JP Pat., 20 043 351 58A, 2004.

241. S. Jing, M. Yan, T. Jing, T. He and Y. Fang, CN Pat., 1 042 829 22B, 2017.

242. K. Kino, M. Kuwahara, T. Ito, F. Hayato, H. Kiyoaki, K. Moriuchi, S. Takasuke and H. Yamaguchi, WO Pat., WO 201 701 015 0A1, 2017.

243. K. Soo and C. Sunghwa, KR Pat., 10 158 040 5B1, 2015.

244. K. Soo and C. Sunghwa, KR Pat., 10 175 104 1B1, 2017.

245. A. R. Winter, US Pat., 8293390B2, 2012.

246. H. Ito and T. Hashimoto, US Pat., 47 328 23A, 1988.

247. S. Zhu, W. Qian, B. Wang, J. Chen and L. Fei, CN Pat., 1 013 252 52B, 2010.

248. B. Wang, Y. Fan, H. Han, D. Xu and X. Cheng, CN Pat., 101847724B, 2013.

249. X. He and Z. Feng, CN Pat., 2 015 230 39U, 2010.

250. H. Zhou, G. Zhang, J. Li, Z. Qin and K. Xue, CN Pat., 1 021 365 93A, 2011.

251. J. T. Clement, D. S. Aaron and M. M. Mench, *J. Electrochem. Soc.*, 2016, **163**, A5220-A5228.

252. Y. A. Gandomi, D. S. Aaron, T. A. Zawodzinski and M. M. Mench, *J. Electrochem. Soc.*, 2016, **163**, A5188-A5201.

253. W. Y. Hsieh, C. H. Leu, C. H. Wu and Y. S. Chen, *J. Power Sources*, 2017, **271**, 245-251.

254. M. Becker, N. Bredemeyer, N. Tenhumberg and T. Turek, *J. Power Sources*, 2016, **307**, 826-833.

255. M. M. Mench, C. Y. Wang and M. Ishikawa, *J. Electrochem. Soc.*, 2003, **150**, A1052-A1059.

256. L. C. Perez, L. Brandao, J. M. Sousa and A. Mendes, 2011, *Renew. Sust. Energ. Rev.*, **15**, 169-185.

257. Q. Dong, M. M. Mench, S. Cleghorn and U. Beuscher, *J. Electrochem. Soc.*, 2005, **152**, A2114-A2122.

258. R. Eckl, R. Grinzinger and W. Lehnert, *J. Power Sources*, 2006, **154**, 171-179.

259. L. A. Schneider, D. Kramer, A. Wokaun and G. G. Scherer, *Electrochem. Commun.*, 2005, **7**, 1393-1397.

260. N. Zamel, A. Bhattarai and D. Gerteisen, *Fuel Cells*, 2013, **13**, 910-916.

261. C. Kalyvas, A. Kucernak, D. Brett, G. Hinds, S. Atkins and N. Brandon, *WIREs Energy Environ.*, 2014, **3**, 254-275.

262. M. Noponen, T. Mennola, M. Mikkola, T. Hottinen and P. Lund, *J. Power Sources*, 2002, **106**, 304-312.

263. P. C. Ghosh, T. Wuster, H. Dohle, N. Kimiaie, J. Mergel and D. Stolten, *J. Power Sources*, 2006, **154**, 184-191.

264. A. B. Geiger, R. Eckl, A. Wokaun and G. G. Scherer, *J. Electrochem. Soc.*, 2004, **151**, 394-A398.

265. C. Wieser, A. Helmbold and E. Gulzow, *J. Appl. Electrochem.*, 2000, **30**, 803-807.

266. M. M. Mench and C. Y. Wang, *J. Electrochem. Soc.*, 2003, **150**, A79-A85.

267. S. J. C. Cleghorn, C. R. Derouin, M. S. Wilson and S. Gottesfeld, *J. Appl. Electrochem.*, 1998, **28**, 663-672.

268. J. T. Clement, T. A. Zawodzinski and M. M. Mench, ECS Trans., 2014, **58**, 9-16.

269. W. He and T. V. Nguyen, *J. Electrochem. Soc.*, 2004, **151**, A185-A195.

270. K. C. Hess, W. K. Epting and S. Litster, *Anal. Chem.*, 2011, **83**, 9492-9498.

271. K. C. Hess, J. F. Whitacre and S. Litster, *J. Electrochem. Soc.*, 2012, **158**, A1351-A1359.

272. Q. Liu, A. Turhan, T. A. Zawodzinski and M. M. Mench, *Chem. Commun.*, 2013, **49**, 6292-6294.

273. K. C. Tully, J. F. Whitacre and S. Litster, *J. Power Sources*, 2014, **248**, 348-355.

274. C. R. Dennison, Y. Gogotsi and E. C. Kumbur, *Phys. Chem. Chem. Phys.*, 2014, **16**, 18241-18252.

275. A. Bhattarai, N. Wai, R. Schweiss, A. Whitehead, G. G. Scherer, P. C. Ghimire and T. D. Nguyen and H. H. Hng, *J. Power Sources*, 2017, **360**, 443-452.

276. E. J. Wilson and C. J. Geankoplis, *Ind. Eng. Chem. Fundamen.*, 1966, **5**, 9-14.

Graphic:

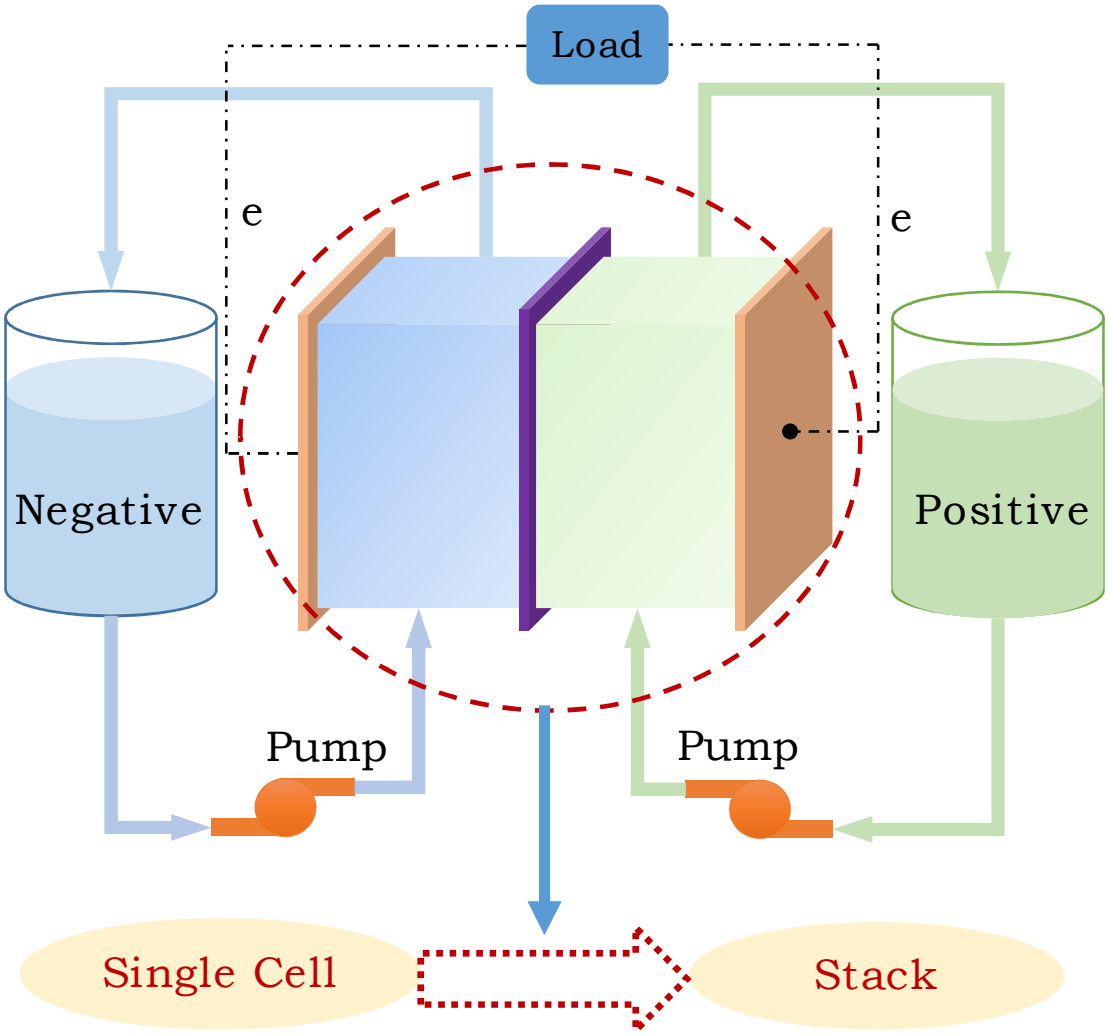

One sentence: This review article summarizes the development of flow fields and stacks, and design considerations for next-generation flow batteries.